# Combination of WENO and Explicit Runge–Kutta Methods for Wind Transport in the Meso-NH Model

THIBAUT LUNET,[a] CHRISTINE LAC,[b] FRANCK AUGUSTE,[c] FLORIAN VISENTIN,[d]
VALÉRY MASSON,[b] AND JUAN ESCOBAR[d]

[a] ISAE-Supaero and CERFACS, Toulouse, France
[b] Centre National de Recherches Météorologiques, Toulouse, France
[c] CERFACS, Toulouse, France
[d] Laboratoire d'Aérologie, Université de Toulouse, CNRS, UPS, Toulouse, France

## ABSTRACT

This paper investigates the use of the weighted essentially nonoscillatory (WENO) space discretization methods of third and fifth order for momentum transport in the Meso-NH meteorological model, and their association with explicit Runge–Kutta (ERK) methods, with the specific purpose of finding an optimal combination in terms of wall-clock time to solution. A linear stability analysis using von Neumann theory is first conducted that considers six different ERK time integration methods. A new graphical representation of linear stability is proposed, which allows a first discrimination between the ERK methods. The theoretical analysis is then completed by tests on numerical problems of increasing complexity (linear advection of high wind gradient, orographic waves, density current, large eddy simulation of fog, and windstorm simulation), using a fourth-order-centered scheme as a reference basis. The five-stage third-order and fourth-order ERK combinations appear as the time integration methods of choice for coupling with WENO schemes in terms of stability. An explicit time-splitting method added to the ERK temporal scheme for WENO improves the stability properties slightly more. When the spatial discretizations are compared, WENO schemes present the main advantage of maintaining stable, nonoscillatory transitions with sharp discontinuities, but WENO third order is excessively damping, while WENO fifth order provides better accuracy. Finally, WENO fifth order combined with the ERK method makes the whole physics of the model 3 times faster compared to the classical fourth-order centered scheme associated with the leapfrog temporal scheme.

## 1. Introduction

Advection schemes play an important role in the numerical models used for computational fluid dynamics. They are a key component of a dynamical core, which solves the fluid dynamic equations in an atmospheric model. A large amount of the literature deals with scalar advection schemes, as it is crucial in representing the transport of tracers and pollutants with a high degree of accuracy and low diffusion. Fewer studies are available for the advection of momentum, even though the flow field is of relevance for all transports in the atmosphere. With momentum advection, the wind field is both the "transporter" and the "transported" field, making the modeling process nonlinear.

Semi-Lagrangian (SL) type schemes have been widely used for wind transport in numerical weather prediction (NWP) models, for example, in the Unified Model (UM; Davies et al. 2005), Applications of Research to Operations at Mesoscale (AROME; Seity et al. 2011), and the Global and Regional Assimilation and Prediction System (GRAPES; Huang et al. 2014), as they are robust and computationally efficient. Standard SL schemes do not conserve mass since they do not use the transport equations in their flux form. However, a new generation of conservative finite-volume SL transport schemes has recently been developed (Zerroukat et al. 2002; Aranami et al. 2015; Shashkin et al. 2016; Erath et al. 2016; Lauritzen et al. 2017). On the other hand, Eulerian schemes are widely used in mesoscale and large eddy simulation (LES) models, in the flux form to ensure conservation. Some of them are fourth-order central advection

Corresponding author: Thibaut Lunet, thibaut.lunet@isae.fr

schemes [as in ARPS; see Xue and Thorpe (1991)], since they present good accuracy and are easy to implement. Nevertheless, the maximum time step size required for their stability is often restrictive. Also, they often require numerical diffusion to avoid energy accumulation at the shortest wavelengths, and a temporal Asselin filter when associated with the leapfrog (LF) temporal scheme.

Another possibility is provided by high odd-ordered (fifth or more) upwind advection schemes, which are often used to improve the computational efficiency, for example, in WRF (Skamarock et al. 2005) and the Lokal Model (LM; Baldauf et al. 2011), as well as the class of essentially nonoscillatory (ENO) and weighted essentially nonoscillatory (WENO) schemes. WENO schemes owe their success to the use of a dynamic set of stencils, where a nonlinear convex combination of lower-order polynomials adapts either to a higher-order upwind approximation at smooth parts of the solution or to a low-order upwind spatial discretization (Jiang and Shu 1995; Shu 1998).

WENO schemes allow a better representation of the solution in the presence of high gradients. Recently, Pressel et al. (2015) have shown the advantages of WENO schemes from 3rd through 11th order for the transport of scalars and momentum over central difference schemes. A major advantage of WENO is its efficiency in suppressing oscillations but it does not guarantee monotonicity of the solution. This is not an issue for momentum transport but it could pose problems for tracer transport when negative tracer densities develop.

WENO spatial discretizations are often combined with explicit Runge–Kutta (ERK) and multistep time-stepping schemes (Shu and Osher 1988). The linear stability of WENO5 has already been studied by Jiang and Shu (1995), Wang and Spiteri (2007), and Motamed et al. (2011) using von Neumann analysis. Originally introduced by Crank and Nicolson (1947), this method has been extensively studied. In particular, Wang and Spiteri (2007) developed criteria for ensuring the existence of a stable Courant–Friedrichs–Lewy (CFL) condition for several ERK–WENO5 combinations, based on Taylor developments in the long wavenumber stability domain. Motamed et al. (2011) extended the methodology to obtain the maximum CFL conditions for a given combination, after assimilating WENO5 to a fifth-order upwind scheme, and comparing spectra of temporal and WENO methods. However, this analysis considered only WENO5, and did not provide stability condition for the ERK method of order strictly greater than 2. Furthermore, the three-stage, third-order strong-stability-preserving ERK (SSP-ERK) method is generally viewed as the reference with WENO5 (Osher and Fedkiw 2003;

Shu and Osher 1988). However, Wang and Spiteri (2007) found temporal discretizations other than the SSP-ERK method to be better suited to WENO5 discretization.

The meteorological model used in this work is Meso-NH, an anelastic research model (Lafore et al. 1998) applied to a broad range of space and time scales. It is a gridpoint Eulerian model using a fourth-order centered advection scheme associated with leapfrog time marching for the momentum components and the piecewise parabolic method (PPM; Colella and Woodward 1984) advection scheme for other variables. Both schemes have proven their accuracy for meteorological simulations (Ricard et al. 2013) but the spatial and temporal schemes for momentum transport strongly limit the time step. Moreover, Meso-NH is increasingly used for large eddy simulations (LESs; Bergot et al. (2015); Dauhut et al. (2015)). LES studies of atmospheric flows have demonstrated how important the numerical methods are for the quality of LES solutions since the work of Ghosal (1996). Kurowski et al. (2014) showed that they are more important than the choice of anelastic or fully compressible equations. Advection plays the primary role in LES as most of the eddies are resolved. Furthermore, LES often deals with sharp gradients, as in the cloud edge region (Baba and Takahashi 2013), or in complex shock-obstacle interactions with an immersed boundary method (Chaudhuri et al. 2011). To meet these objectives, a first attempt was made using PPM for momentum in Meso-NH, as it is already used in the model for scalar variables and has demonstrated good conservative properties. However, the C grid imposed multiple averaging to adapt PPM for flux variables, and induced a significant loss of accuracy, making PPM worse than the fourth-order centered advection scheme for wind transport. WENO schemes were therefore of great interest in avoiding generating spurious numerical oscillations around sharp gradients so WENO simulations of third and fifth order were implemented in Meso-NH.

Here, we aim to give a more complete picture of the stability of WENO5 and WENO3 combined with ERK methods in a meteorological model like Meso-NH with a clear objective of finding an optimal combination in terms of wall-clock time to solution and accuracy. The objective is to find the time integration method allowing the higher CFL number (around 2 at minimum) with WENO schemes for momentum transport, so that the cost of simulation, including physics modeling, is much cheaper. The classical fourth-order centered schemes associated with the LF temporal scheme will be used as a reference basis to evaluate the WENO schemes. WENO3 is already known to be excessively damping (Tan et al. 2005).

The aim of the WENO5 method is to reduce the gap with the fourth-order centered advection scheme in

terms of implicit numerical diffusion, while retaining a good stability condition with the CFL number. First, the von Neumann stability analysis will be applied to the WENO schemes and to the several ERK methods.

It is also well known that an advection scheme may work very well on some test problems but fail on others (Tan et al. 2005). The test cases presented here are of increasing complexity. They are first taken from a standard set of test problems for dynamical cores: mountain wave flow in the hydrostatic regime and buoyancy-driven flow. Then, they address meteorological applications including all the physics and sharp gradients, like LES of fog and mesoscale windstorm simulation. Throughout this study, several combinations of WENO-ERK methods are investigated and selected to determine the optimal combination for the two WENO schemes. A good way of measuring implicit numerical diffusion is by determining the smallest resolved wavelength, defined as the effective resolution (Skamarock 2004; Ullrich 2014). Increasing the effective resolution of a model by using higher-order numerical methods might prove more beneficial in terms of precision than simply increasing the grid resolution, supposing that relevant finescale structures are larger than the grid scale. This method will be applied to the meteorological test cases.

The remainder of this paper is organized as follows. Section 2 describes the wind advection equations and the spatial and temporal discretizations for the different numerical methods. A von Neumann stability analysis is then conducted for WENO schemes. Section 3 discusses the evaluation of the numerical schemes for four test cases. Finally, section 4 summarizes the key findings of this research and proposes future directions of inquiry.

## 2. Theoretical analysis

### a. General approach

Among all variables solved by a meteorological model, the three-dimensional vectorial velocity field and its modification through advection is the main focus here. In Meso-NH, the equations for the wind in their flux form, considering only advection, are as presented below:

$$\frac{\partial \rho u}{\partial t} = -\frac{\partial(\rho U^c u)}{\partial x} - \frac{\partial(\rho V^c u)}{\partial y} - \frac{\partial(\rho W^c u)}{\partial z}, \qquad (2.1)$$

$$\frac{\partial \rho v}{\partial t} = -\frac{\partial(\rho U^c v)}{\partial x} - \frac{\partial(\rho V^c v)}{\partial y} - \frac{\partial(\rho W^c v)}{\partial z}, \quad \text{and} \qquad (2.2)$$

$$\frac{\partial \rho w}{\partial t} = -\frac{\partial(\rho U^c w)}{\partial x} - \frac{\partial(\rho V^c w)}{\partial y} - \frac{\partial(\rho W^c w)}{\partial z}, \qquad (2.3)$$

where $u$ and $v$ are the two horizontal velocities and $w$ the vertical velocity. In addition, $\rho$ is the density value, which
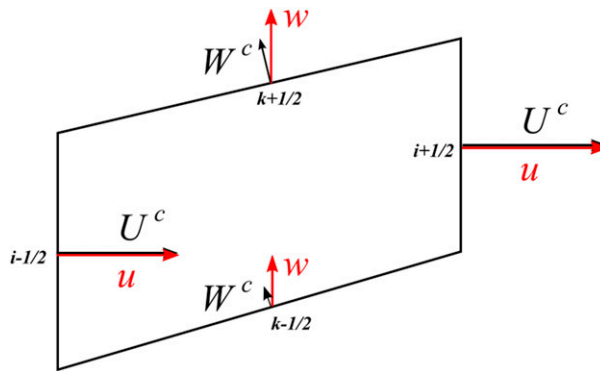


FIG. 1. Representation of contravariant components of the wind $U^c$, $V^c$, and $W^c$ on the C grid in a 2D vertical plane.

varies only with altitude, considering the anelastic approximation. The anelastic equations of Meso-NH are formulated according to Durran (1989) or Lipps and Hemler (1982) and the system of Durran (1989) will be used in this study. As a result of the conformed horizontal projection and terrain-following vertical coordinates such as have been proposed by Gal-Chen and Somerville (1975) or Schär et al. (2002), the contravariant components of the wind $U^c$, $V^c$, and $W^c$ are introduced, corresponding to the components of the wind orthogonal to the coordinate lines (Fig. 1, keeping in mind that contravariant components are not actually vectors). Within the Cartesian framework, metric terms exactly cancel out, and $U^c$, $V^c$, and $W^c$, are equal to $u$, $v$, and $w$. Hence, the advection scheme transports the directional momentum (the "advected" field) by the contravariant components of the wind field (the "advector" field).

To solve (2.1)–(2.3), Meso-NH uses the so-called method of lines, which consists of discretizing the spatial terms of each equation (right-hand terms) in order to obtain a linear system of three ordinary differential equations (ODEs) in time. A time integration will then be applied to find the approximate solution. For the sake of simplicity, this study will consider only the $x$-momentum equation and its $x$-derivative term:

$$\frac{\partial(\rho U^c u)}{\partial x} = \frac{\partial[F_C(\rho U^c)F(u)]}{\partial x}, \qquad (2.4)$$

where $F_C(\rho U^c)$ contains the topologic terms, which integrate terrain transformations. The second flux $F(u)$ is calculated on the mesh point without considering terrain transformation, using the advection method. All other derivative terms are built with a similar methodology.

### b. Spatial discretization

Because of the Arakawa C grid, the advector (contravariant components) and the transported wind field

($u$, $v$, and $w$) represent different directions. The discrete form of the contravariant metric term is of fourth order in the vertical direction, in agreement with Klemp et al. (2003), but of second order in the horizontal directions.

Defining $i$ as the spatial index in the $x$ direction and $\Delta x$ as the mesh step size, the derivative is written such that

$$\frac{\partial(\rho U^c u)_i}{\partial x} = \frac{F(u)_{i+1/2} F_C(\rho U^c)_{i+1/2}}{\Delta x} - \frac{F(u)_{i-1/2} F_C(\rho U^c)_{i-1/2}}{\Delta x}. \quad (2.5)$$

Then, a chosen discretization is applied to the flux terms $F$, following its definition using the flux formulation:

$$\frac{\partial u_i}{\partial x} = \frac{F(u)_{i+1/2} - F(u)_{i-1/2}}{\Delta x}. \quad (2.6)$$

Three different methods are used to discretize $F$: WENO discretization of fifth and third order (WENO5 and WENO3, respectively) and a centered discretization of fourth order (CEN4TH).

### 1) DISCRETIZATION WITH WENO5

The first step consists of separating the velocity flux terms into positive and negative fluxes, using Lax–Friedrich flux splitting as in Shu (1998):

$$F_{\text{WENO}}(u)_{i+1/2} = f^+_{i+1/2} + f^-_{i+1/2}. \quad (2.7)$$

In the following development, only the reconstruction of positive fluxes will be described. The reader is invited to refer to Wang and Spiteri (2007), Shu (1998), and Castro et al. (2011) for a more detailed description. The velocity fluxes are constructed employing a stencil given by a Lagrangian interpolation using the velocity average on each cell:

$$\begin{aligned} f^+_{i+1/2} = &\gamma_0 \left( \frac{2}{6}\overline{u}_{i-2} - \frac{7}{6}\overline{u}_{i-1} + \frac{11}{6}\overline{u}_i \right) \\ &+ \gamma_1 \left( -\frac{1}{6}\overline{u}_{i-1} + \frac{5}{6}\overline{u}_i + \frac{2}{6}\overline{u}_{i+1} \right) \\ &+ \gamma_2 \left( \frac{2}{6}\overline{u}_i + \frac{5}{6}\overline{u}_{i+1} - \frac{1}{6}\overline{u}_{i+2} \right) \end{aligned} \quad (2.8)$$

with the average value of the velocity defined by

$$\overline{u}_i = \frac{1}{\Delta x_i} \int_{x_{i-1/2}}^{x_{i+1/2}} u(\xi)\, d\xi. \quad (2.9)$$

The strength of the WENO-5 method rests on the choice of the WENO stencil weights, $\gamma_j$. These allow a nonoscillatory solution to be kept even in the presence of shock or a high gradient in the velocity field. These stencil weights are fully described in appendix A.

### 2) DISCRETIZATION WITH WENO3

As for WENO5, WENO3 is fully described by Shu (1998). Third-order positive fluxes are defined by

$$f^+_{i+1/2} = \gamma_0 \left( -\frac{1}{2}\overline{u}_{i-1} + \frac{3}{2}\overline{u}_i \right) + \gamma_1 \left( \frac{1}{2}\overline{u}_i + \frac{1}{2}\overline{u}_{i+1} \right). \quad (2.10)$$

The WENO3 stencil weights are fully described in appendix A.

The computational cost of WENO3 is lower than that of WENO5, but WENO3 is known to be more diffusive for advection problems, as observed by Tan et al. (2005). This aspect will be studied further in the following sections.

### 3) DISCRETIZATION WITH CEN4TH

For CEN4TH, no flux decomposition is required. The fluxes are directly computed using a fourth-order reconstruction:

$$F_{\text{CEN4TH}}(u)_{i+1/2} = \frac{7(u_{i+1} + u_i) - (u_{i+2} + u_{i-1})}{12}. \quad (2.11)$$

CEN4TH reverts to a second-order centered scheme at the edges of the computational domain (for open boundary conditions only). It must also be combined with a numerical diffusion operator of fourth order in the model, in order to damp numerical energy accumulation in the shortest wavelengths. This operator is fully described in appendix B.

### c. Temporal discretization

### 1) EXPLICIT RK METHOD

Once the space derivatives have been estimated, a temporal discretization is used to integrate in time from the current state to the next one. For CEN4TH, the temporal discretization is based on the leapfrog method, while the rest of the model uses the forward-in-time (FIT) method. For WENO schemes, the leapfrog method is unstable in the model. Therefore, ERK methods of higher order are favored, together with FIT time integration for the rest of the model [contravariant flux $F_C(\tilde{\rho}U^c)$ among others]. The general temporal process for one advection term in (2.1) will then be described.

Using the anelastic hypothesis ($\partial\rho/\partial t = 0$), we consider the tendency of a variable defined by its time variation induced by the spatial term in the advection equation, noted $T_u$,

$$T_u = \rho \frac{\partial u}{\partial t}, \qquad (2.12)$$

which is written in discrete form using the FIT formulation (with $n$ as the temporal index):

$$T_u^{n+1} = \rho \frac{u^{n+1} - u^n}{\Delta t}. \qquad (2.13)$$

The contravariant flux $F_C (U^c)$, that is, the advection field, is kept constant over the time step, to satisfy the continuity equation. The ERK method is applied to the following equation:

$$\rho \frac{\partial u}{\partial t} = M(u) + S, \qquad (2.14)$$

where $M(u)$ is the discrete term defined in (2.6) and $S$ represents the other terms of the momentum equation (source, diffusive terms, etc.). We consider a general s-stage ERK method defined by its Butcher coefficients:

$$\begin{array}{c|ccccccc} c_1 & & & & & & \\ c_2 & a_{21} & & & & & \\ c_3 & a_{31} & a_{32} & & & & \\ c_4 & a_{41} & a_{42} & a_{43} & & & \\ \vdots & \vdots & \vdots & \vdots & \ddots & & \\ c_s & a_{s1} & a_{s2} & a_{s3} & \cdots & a_{s,s-1} & \\ \hline & b_1 & b_2 & b_3 & \cdots & b_{s-1} & b_s \end{array} \quad .$$

The advection tendency follows:

$$u_1^n = u^n$$

$$u_k^n = u^n + \Delta t \sum_{j=1}^{k-1} a_{k,j} \frac{M(u_j^n) + S}{\rho^n}$$

$$T_u^{n+1} = \sum_{k=1}^{s} b_k [M(u_k^n) + S]. \qquad (2.15)$$

Adding the advection tendency to obtain $u^{n+1}$ using (2.13) leads to the classical Runge–Kutta method applied to the momentum equation. The different explicit RK methods considered in this study are presented below (see appendix D).

### 2) ADDITIONAL TIME-SPLITTING METHOD

To increase the maximum CFL number, an additional time-splitting step is introduced for the wind advection. One time step $[t_n, t_{n+1}]$ is divided into $L$ regular substeps $[t_l, t_{l+1}]$ with $t_n = t_0 < \cdots < t_l < t_{l+1} < t_L = t_{n+1}$. Once one value $u^l$ is known ($u^0$ at first), the next value $u^{l+1}$ is computed using (2.13) with $\Delta t = t_{l+1} - t_l$, which gives

$$T_u^{l+1} = \rho \frac{u^{l+1} - u^l}{\Delta t} \qquad (2.16)$$

with $u^{l+1}$ computed using all stages of the ERK method as described in (2.15). This process is repeated $L$ times to compute the $L$ tendencies. In the end, the tendency of the original final time $t_{n+1}$ is obtained with an average:

$$T_u = \frac{1}{L} \sum_{l=1}^{L} T_u^l. \qquad (2.17)$$

The gain in terms of stability will be studied in section 3.

### d. Temporal scheme for the rest of the model

The other prognostic variables of Meso-NH (potential temperature, mixing ratios, turbulent kinetic energy, scalars) are transported with a monotonic version of the PPM (Colella and Woodward 1984; Carpenter et al. 1990), with FIT time marching. With respect to a CFL of strictly <1 for PPM (a threshold of 0.8 is proposed), a time-splitting step is also added to the advection of scalar variables.

Hence, to summarize the time marching in Meso-NH, three time steps are effective when WENO schemes are applied to momentum transport (Fig. 2a). The larger time step is applied to the whole model including the physics and the pressure solver, with the FIT temporal scheme. The advection of all variables is conducted with a constant advection momentum vector. A smaller time step is used for wind advection when applying the ERK method on the subinterval. Another smaller time step is used for scalar advection, to ensure a CFL of strictly less than 1 for PPM. This smaller time step for PPM can evolve during the run as a function of the CFL number.

With the centered momentum transport scheme, a single time step is considered as the CFL number and is always strictly <1, with FIT time marching for the whole model except for wind advection, which uses the leapfrog temporal scheme (Fig. 2b).

### e. Von Neumann stability analysis

### 1) MOTIVATIONS

When the Runge–Kutta scheme is combined with WENO schemes, one useful method for investigating stability remains the von Neumann analysis. As an introduction, von Neumann analysis principles will be briefly summarized, based on the developments in Motamed et al. (2011) and the generalization of the
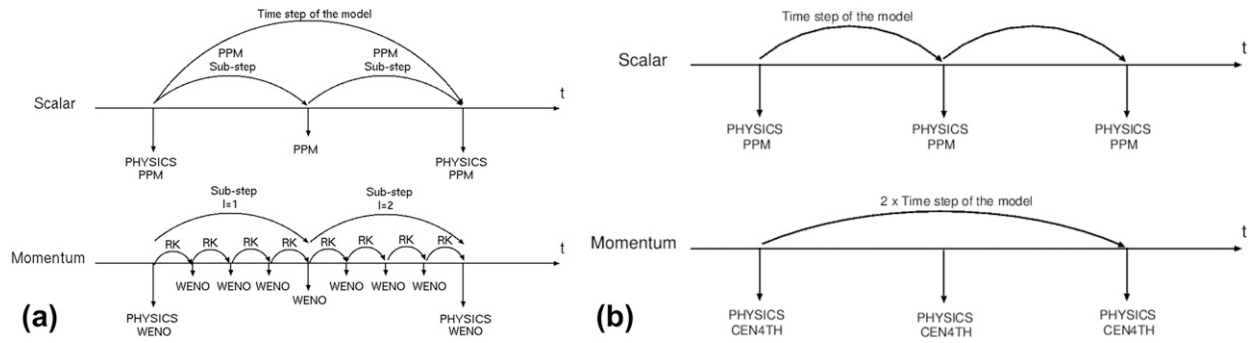
FIG. 2. Representation of the time marching in Meso-NH with (a) WENO and (b) CEN4TH/leapfrog schemes for the transport of momentum.

analysis for common space–time schemes in Baldauf (2008). Then, a new graphical representation of linear stability will be proposed, in order to determine maximum CFL stability conditions along with the diffusion error when considering the space–time discretization combination. This allows for discrimination among several ERK methods in an attempt to find the best combination for both WENO3 and WENO5.

### 2) VON NEUMANN ANALYSIS

Considering one dimension (with $j$ as the spatial index), a constant value of contravariant velocity and density is taken during a time step. This method, also called the frozen coefficient method, is classically used to adapt the linear von Neumann analysis to nonlinear equations (Feistauer et al. 2003). Equation (2.1) is then simplified as

$$\frac{\partial u}{\partial t} = -U^c \frac{\partial u}{\partial x} \simeq -U^c \frac{F(u)_{j+1/2} - F(u)_{j-1/2}}{\Delta x} = M(u). \quad (2.18)$$

Assuming periodic boundary conditions and using a discrete Fourier transform in space, the semidiscrete solution of (2.18) is written as

$$u_j(t) = \sum_{\kappa=-N/2}^{N/2} \hat{u}_\kappa(t) e^{i\omega_\kappa j \Delta x}, \quad (2.19)$$

where $j$ corresponds to the spatial index in the $N$-points mesh and $\omega_k$ is the spatial frequency associated with $\hat{u}_k$. Because of the linearity of (2.18) and by the superposition principle, it is possible to focus on only one term of the sum:

$$u_j(t) = \hat{u}_\kappa(t) e^{ij\theta_\kappa}, \quad \theta_\kappa = \omega_k \Delta x, \quad (2.20)$$

where $\theta_\kappa$ is the wavenumber considered. The operator $M$ in (2.18) can be written as

$$M(u_1, \ldots, u_j, \ldots, u_N) = -\frac{z_{\text{WENO}}(\theta_\kappa) u_j}{\Delta x}, \quad (2.21)$$

where $z_{\text{WENO}}$ corresponds to the Fourier symbol of the spatial operator $M$. As in Motamed et al. (2011), the analysis is conducted here by considering a smooth solution, and the WENO discretization is linearized to obtain the Fourier symbols described in appendix C.

Applying an ERK method to the semidiscrete equation in (2.18) leads to

$$u_j^{n+1} = g(\hat{z}_k) u_j^n, \quad \text{with} \quad \hat{z}_k = -\text{CFL} z_{\text{WENO}}(\theta_\kappa), \quad (2.22)$$

where $n$ corresponds to a temporal index and the CFL number $U^c \Delta t / \Delta x$. The function $g$ is the ERK amplification factor.

As developed by Wang and Spiteri (2007), noting the matrix **A** and the vector **b** as the coefficients $(a_{i,j})$ and $(b_i)$ respectively, of the Butcher table of the $s$-stage ERK method of order $p$, $g$ can be expressed as

$$g(\hat{z}) = 1 + \sum_{l=1}^{p} \frac{\hat{z}^l}{l!} + \sum_{l=p+1}^{s} \hat{z}^l \mathbf{b}^{\text{T}} \mathbf{A}^{l-1} \mathbf{e}, \quad (2.23)$$

where **e** corresponds to the unity vector of size $s$. From this, the CFL stability condition can be expressed as

$$\text{CFL stable} \Leftrightarrow \forall \quad \theta_\kappa \in [0, \pi], \quad |g(\hat{z})| \leq 1. \quad (2.24)$$

Values of $\theta_\kappa$ are taken only in $[0, \pi]$ because of the symmetry implied by the Fourier transform of the real field $u$. Using (2.24), a general method can be developed to find the maximum stable CFL for all types of linear spatial discretizations combined with all ERK methods.
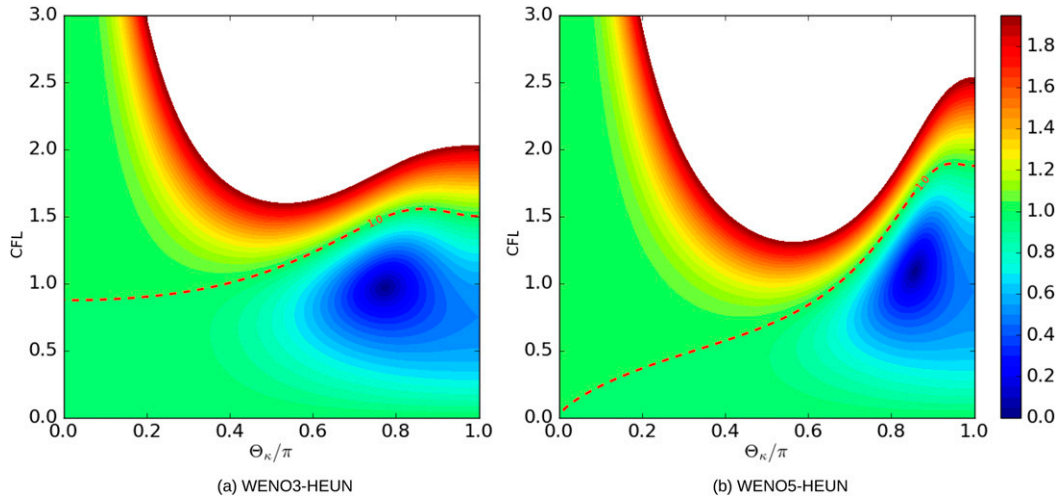
FIG. 3. Stability contours for (left) WENO3 and (right) WENO5 combined with the HEUN method.

The latter are fully described in appendix D, but a short description is given below:

- FE, forward Euler method (one stage, order 1);
- RK21, two stages, order 1;
- HEUN2, Heun method (two stages, order 2) (Süli and Mayers 2003);
- RK33, strong-stability-preserving (SSP) method, three stages, order 3;
- RK53, five stages, order 3; and
- RKC4, classical ERK method (four stages, order 4).

### 3) EXTENSION OF THE ANALYSIS FOR WENO3 AND WENO5 SCHEMES

The condition (2.24) can be represented graphically, using a two-dimensional contour plot of $|g(\theta_\kappa, \text{CFL})|$. Examples of these representations, which will be called stability contours hereafter, are given in Fig. 3.

The primary goal of the stability contours is to determine the maximum stable CFL number for a given combination of time and space discretizations. It can be defined as the ordinate of the highest horizontal line that does not cross the isocontour line $S$, which is defined as follows:

$$S = [(\theta_\kappa, \text{CFL})/|g(\theta_\kappa, \text{CFL})| = 1]. \quad (2.25)$$

(The representation of such contours is given in Fig. 3 using a standard isocontour plotting function.) This is actually a direct application of (2.24) to the stability contour, which can be posed as

$$\text{CFL}_{\max} = \max[\text{CFL}/\forall \theta_\kappa \in [0, \pi], |g(\text{CFL}, \theta_\kappa)| \leq 1]. \quad (2.26)$$

Figure 3 shows how the stability condition changes with the order of the space discretization for one given time discretization method. It also shows a good representation of the diffusion properties of the scheme combination, considering one given CFL number. The von Neumann analysis was performed considering a pure advection problem. In that case, diffusion is only brought by the numerical schemes. The closer $|g(\theta_\kappa, \sigma)|$ is to 1 (shown in green in Fig. 3), the smaller are the diffusion errors the numerical method makes. In contrast, $|g(\theta_\kappa, \sigma)|$ close to 0 (blue color in Fig. 3) indicates a damping of the corresponding wavenumber $\kappa$, which will induce a diffusion error in this wavenumber domain. Figure 4 shows the combination of WENO5 with the RK33 and RK53 time integrations. Considering a unitary CFL number, the amplitude of the wavenumber component is divided by two in one time step at around $\kappa > 0.60\pi$ for RK33, and around $\kappa > 0.70\pi$ for RK53. So, the error in the high-wavenumber domain is smaller for RK53 than for RK33, despite the fact that both methods are of the same order.

The stability contour study methodology was used to compare the different combinations of ERK methods with WENO schemes. Maximum stable CFLs (CFL$_{\max}$) are represented in Table 1 and several conclusions can be drawn, from the table and the stability contours:

- WENO3 with forward Euler and WENO5 with forward Euler and the second-order RK method are linearly unstable, in agreement with the findings of Spiteri and Ruuth (2002).
- WENO3 requires at least two stages to achieve stability with CFL $\geq$ 1.0, while WENO5 requires mostly three stages.
- For a given ERK method, the diffusion error for a small wavenumber is smaller for the WENO5 method than for WENO3.
- RK53, RKC4, and RK33 for WENO schemes can be ranked in this order for efficiency (i.e., in order of
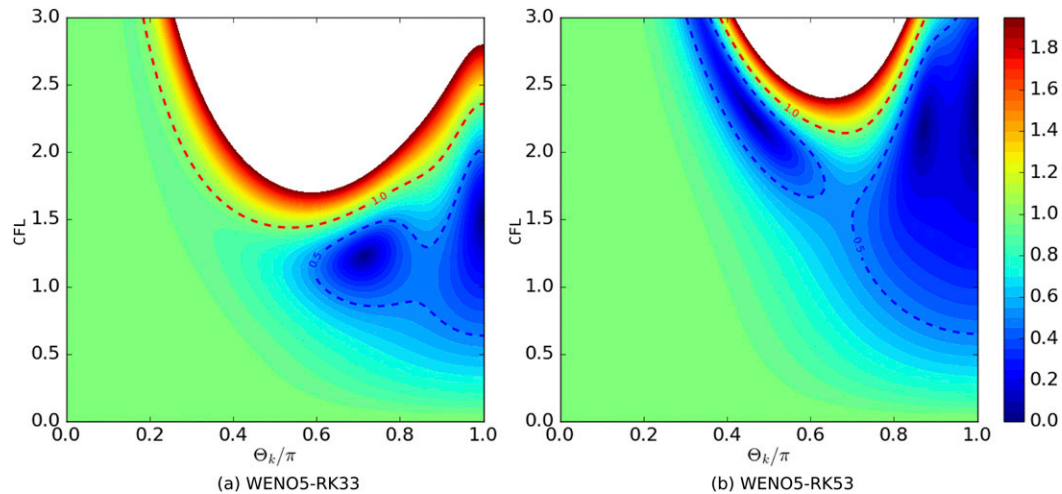
FIG. 4. Stability contours for WENO5 combined with (left) RK33 and (right) RK53.

maximum CFL numbers). The relatively smaller CFL$_{max}$ with RK33 is in agreement with Wang and Spiteri (2007), who have shown linear instability with RK33 for CFL numbers above 1.43 and the superiority of RK53 over RK33.

- The diffusion error for small wavenumbers is smaller when both the order and the number of stages increase.

To conclude on this section, the numerical analysis pointed out that some ERK methods (RK53 and RKC4, as well as RK33) are better adapted to WENO schemes in terms of stability. The FE and HEUN2 temporal schemes will be discarded for the rest of the paper.

These results were achieved with the assumption of linearity and without considering the impact of the generalized coordinates through the contravariant components. In the next section, the different numerical schemes will be evaluated on more complete test cases taking into consideration the previously mentioned points, and comparisons will be made with the von Neumann analysis results.

## 3. Numerical results

### a. Hydrostatic mountain waves

Hydrostatic mountain waves are a classical test for the advection topic, which handles orography. This test involves the steady-state solution of linear 2D hydrostatic flow over a single-peaked mountain with constant inflow, as in Durran and Klemp (1983) and Xue and Thorpe (1991). The profile of the symmetric Witch of Agnesi mountain is used as

$$h(x) = h_{max}\frac{a^2}{x^2 + a^2}$$

with $h_{max} = 1$ m as the height and $a = 10$ km the half-width of the mountain. The initial state of the atmosphere is a constant mean flow with $U = 20\,\mathrm{m\,s}^{-1}$, a ground potential temperature of $\theta = 250$ K, and a Brunt–Väisälä frequency of $N = 0.2\,\mathrm{s}^{-1}$. The resolutions are $\Delta x = 500$ m and $\Delta z = 250$ m, and the domain extends horizontally over 800 km and vertically over 30 km. A Rayleigh damping layer is applied above 22 km. Figure 5 shows that the numerical (dashed gray) values of vertical velocity and the analytical (colored contours) values compare well. The simulation is given only for the WENO5 scheme here, as the differences with various advection schemes are too tiny to be visible.

A stability study was conducted, including the additional time-splitting step for WENO schemes, and maximum CFL number and the effective CFL number (CFL divided by the number of RK stages) are presented in Table 2. Without time splitting, the maximum CFL numbers of the hydrostatic case are lower than for the linear results in Table 1. With time splitting, WENO3 achieves an equivalent maximum CFL number for RK53, and even better results for RKC4, compared to the linear stability analysis. WENO5 produces similar maximum CFL numbers with RKC4 and RK53 (lower than for the linear case with RK53).

TABLE 1. Maximum CFL number for WENO schemes combined with different ERK methods according to the stability contour study from the von Neumann analysis.

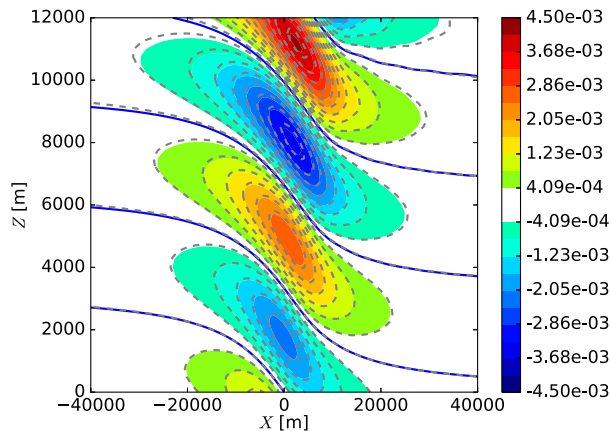|  | FE | RK21 | HEUN2 | RK33 | RK53 | RKC4 |
|---|---|---|---|---|---|---|
| CFL$_{max}$ |  |  |  |  |  |  |
| WENO5 | 0.00 | 0.78 | 0.00 | 1.44 | 2.14 | 1.73 |
| WENO3 | 0.00 | 0.76 | 0.87 | 1.63 | 2.30 | 1.75 |

FIG. 5. Case of a linear hydrostatic mountain. Vertical cross-section of vertical velocity (m s$^{-1}$) after 10 h. Colored isovalues correspond to the analytical solution and dashed gray lines to the numerical one, given here for WENO5 and RK53, with CFL = 0.4.

TABLE 2. Case of linear hydrostatic flow: maximum CFL number with maximum effective CFL number (CFL number divided by the number of stages) in italics for CEN4TH and for WENO schemes combined with ERK methods and additional time splitting ($L$ is the split number).

| | LF | RK33 | RK53 | RKC4 |
|---|---|---|---|---|
| CEN4TH | 0.4 | | | |
| WENO5 | | | | |
| $L = 1$ | | 1.0 | 1.4 | 1.4 |
| | | *0.33* | *0.28* | *0.35* |
| $L = 2$ | | 1.7 | 1.8 | 1.8 |
| | | *0.28* | *0.18* | *0.23* |
| $L = 3$ | | 1.7 | 1.8 | 1.8 |
| | | *0.18* | *0.12* | *0.15* |
| WENO3 | | | | |
| $L = 1$ | | 1.0 | 1.3 | 1.3 |
| | | *0.33* | *0.26* | *0.33* |
| $L = 2$ | | 2.1 | 2.5 | 2.5 |
| | | *0.35* | *0.25* | *0.31* |
| $L = 3$ | | 2.1 | 2.5 | 2.6 |
| | | *0.23* | *0.17* | *0.22* |

RK33 presents the smallest CFL numbers but the highest effective CFL numbers. However, the cost of an ERK method is not only limited to its efficiency: as represented in appendix D, RK33 requires more memory storage than the RKC4 and RK53 methods, as the latter have a diagonal Butcher matrix; so, they only need to store one field in memory at each stage to compute the next field. RK33 has a plain Butcher matrix, so it requires as many fields to be stored in memory as the number of stages (three here) needed to compute the final solution.

Concerning the split number for both WENO schemes, the additional two-time splitting steps yield an improvement in the maximum CFL number of around a factor of 2, while the effective maximum CFL number is reduced. There is still one exception for RK33–WENO3 for which the two time-splitting steps allows an increase in the maximum effective CFL. Three time-splitting steps add nothing more to the maximum CFL number compared to the two time-splitting steps.

To conclude, this test allowed the results of the previous von Neumann analysis to be assessed. Even if the theory did not reproduce exactly the same CFL limitations, they were fairly well reproduced for the 2D hydrostatic case. Two arguments have been shown to favor a combination of RKC4 and RK53 with WENO5 compared to RK33 in the rest of the study: the maximization of the CFL number allows a bigger time step to be used to minimize the cost of the rest of the model (physics, pressure solver, etc.) and minimizes the memory storage.

### b. The density current test case

The popular density current test case (buoyancy-driven flows class) was proposed by Straka et al. (1993), who described the conditions and hypothesis. It involves the study of a cold-air bubble falling in idealized atmospheric conditions and followed in time by the development of a gravity current above an ideal surface. The stratification is neutral, with a potential temperature equal to the surface temperature of 300 K. To illustrate the dynamics studied, Fig. 6 shows the evolution of the potential temperature (obtained with the reference simulation detailed in appendix E). During the first 3 min, and as a result of the buoyancy effects, the cold-air bubble falls. After these first few minutes, the bubble interacts with the nonpermeable ground and shifts the global vertical movement toward a horizontal displacement, inducing a cold front. After 9 min, three vortices are clearly visible and the front location covers a distance greater than 15 km. We focus our attention on the end of the period ($t = 900$ s) and we study local and integrated variables:

- extreme values of the $\theta$ temperature: $\Delta\theta_{min} = \theta_{min} - 300$;
- extreme values of the $\mathbf{u}$ velocity vector: $u_{min}$, $u_{max}$, $v_{min}$, and $v_{max}$ (horizontal and vertical directions);
- total kinetic energy: $E_k = \iiint e_k \, dV$, where $e_k = (1/2)\|\mathbf{u}\|^2$; and
- total enstrophy: $E_s = \iiint e_s \, dV$, where $e_s = (\nabla \times \mathbf{u})^2 = \|\boldsymbol{\omega}\|^2$.

The converged solution in time and in space noted REFO is described in appendix E and shows good agreement with previous studies. In this section, the impact of the three momentum advection schemes and associated temporal algorithms is estimated: CEN4TH (leapfrog), WENO3(RK21) and WENO5(RK53). No time splitting is added for the ERK methods ($L = 1$).
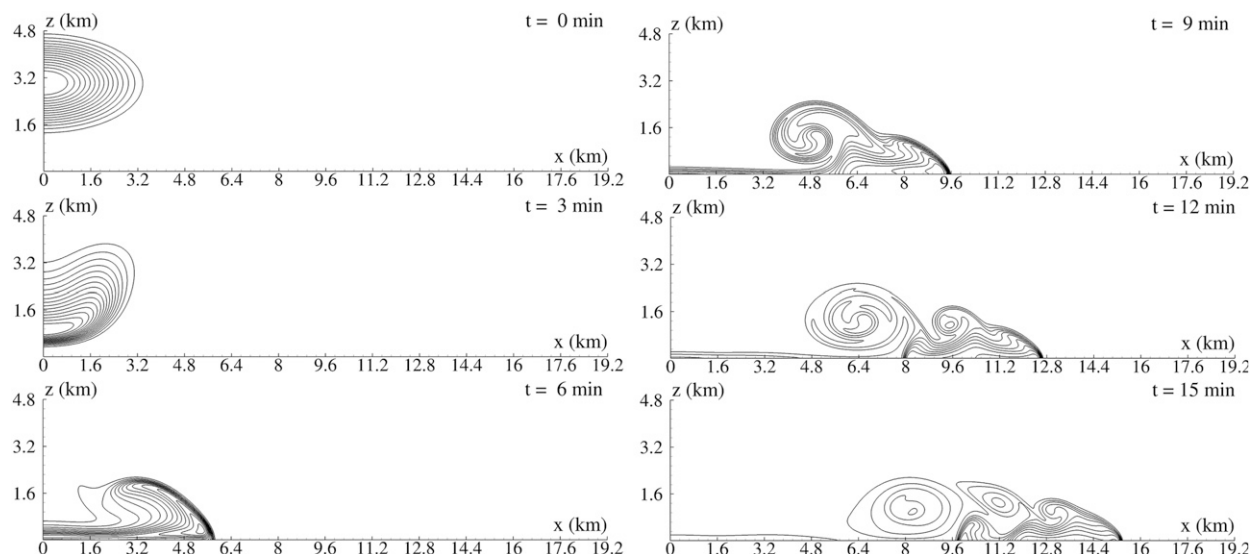
FIG. 6. Snapshots of the potential temperature field at six times (MNH-REF0 resolution): $t = 0, 3, 6, 9, 12,$ and 15 min. Sixteen isocontours are drawn with a 1-K contour interval ($\theta_{min} = 284$ K, $\theta_{max} = 299$ K).

The nondimensional space (time) step is defined as $\Delta X^*/\Delta x_{ref}$ ($\Delta T^* = ||\mathbf{u}||\Delta t/\Delta x$). The minima of the non-dimensional space and time steps used in REF0 (see appendix E) are $\Delta X^* = 1$, $\Delta T^* = 0.15$.

1) COMPARISON OF TWO DISCRETIZATIONS

Two spatiotemporal resolutions are detailed: fine ($\Delta X^* = 2$, $\Delta T^* = 0.2$) and coarse ($\Delta X^* = 8$, $\Delta T^* = 0.4$). Figure 7 illustrates the fields of $\theta$ (panel a), $e_k$ (panel b), and $e_s$ (panel c) obtained with the reference (top panels), the fine (middle panels), and the coarse (bottom panels) resolutions. For the fine resolution, all advection schemes show visual and qualitative similarities with REF0. The density current preserves its shape and covers the same horizontal distance (Fig. 7a, top and middle panels). It exhibits the vortex shedding of three rotors (Fig. 7c, top and middle panels) and illustrates the vorticity production at the head of the cold front as a result of a strong shear acting in this region (the $e_s$ maximum is contained in the boundary layer separating the cold front from the undisturbed region). The middle panel in Fig. 7b highlights the location of the $e_k$ maximum in the first rotor developed in time.

When the resolution becomes coarser (Fig. 7, bottom panels) the density current loses some of its expected characteristics. The front shape exhibits only two rotors with CEN4TH and WENO5; the second rotor tends to disappear with WENO3. The $e_k$ field in the bottom panels of Fig. 7b reveals, especially for WENO3, the impact of the numerical dissipation leading to a decrease in kinetic energy. The $e_k$ maximum is always detected in the first rotor and a loss of $e_s$ is visible at the front head. Therefore, the

spatial resolution has become too coarse to capture the shear in the boundary layer responsible for the growth of Kelvin–Helmholtz instability. The first rotor (compared to the second and the lost third rotors) corresponds to the part of the gravity current that resists best (creation of the first rotor at $t \sim 450$ s by a front with a vertical thickness approximately twice that of the front at $t \sim 900$ s).

Table 3 summarizes all the variables studied and obtained by the simulations using the fine and coarse resolutions, depending on the advection schemes. Boldface characters in Table 3 indicate the results giving the lowest relative error compared to REF0. Values of the fine-resolution results highlight good agreement between WENO5, CEN4TH, and REF0. Considering all the variables, WENO3 presents the most significant differences. The bottom of Table 3 emphasizes the results obtained with coarse resolution. These results show the best adequacy on $\Delta\theta_{min}$, $u_{min}$, $v_{min}$, $v_{max}$, and $\omega_{max}$ between the reference and WENO5. On $u_{max}$, $x_{front}$, $E_k$, and $E_s$, CEN4TH shows the lowest relative error with respect to the REF0 values. Once more, the observed deviation from the reference solution appears to be the greatest with the overdiffusive WENO3.

To add a comment, $u_{max}$ is observed not to be related to the front location here, which mostly reflects the well-designed first rotor. In the same way, the $\omega_{max}$ location is in the front (rear) rotor for the fine (coarse) resolution. This shows, first, that the scales of the front head are much more complicated and difficult to capture with regard to its wake and, second, our interest in describing the problems associated with several local variables because of the difficulty in distinguishing the most pertinent among them.
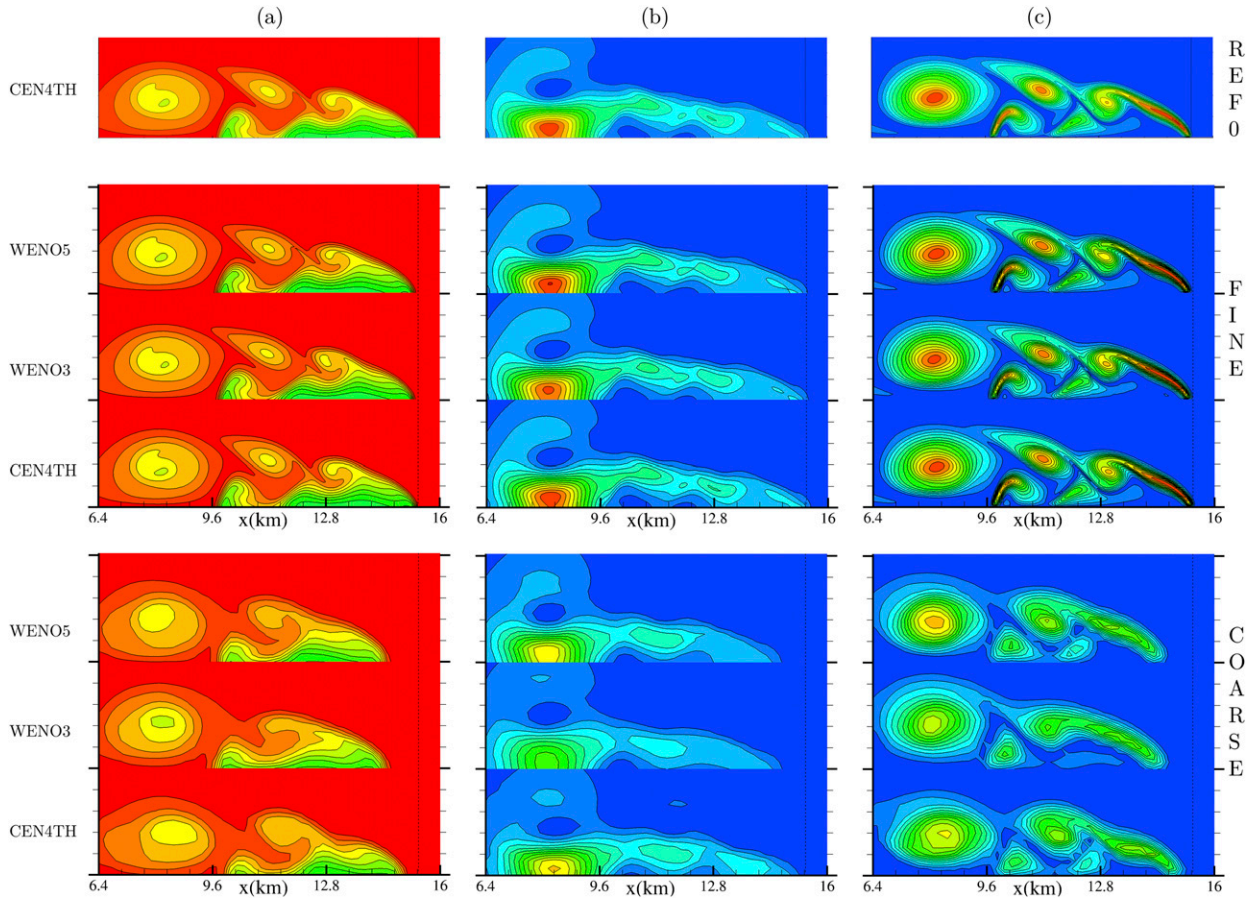
FIG. 7. Sixteen isocontours at $t = 900$ s depending on the advection schemes (WENO3, WENO5, and CDN4TH) of (a) the potential temperature ($\theta_{min} = 284$ K, $\theta_{max} = 299$ K), (b) the kinetic energy ($e_{k,max} = 600$ m$^2$ s$^{-2}$), and (c) the enstrophy ($e_{s,max} = 0.074$ m$^2$ s$^{-2}$). (top) The REF0 reference simulation ($\Delta X^* = 1$, $\Delta T^* = 0.15$), (middle) the fine spatiotemporal resolution ($\Delta X^* = 2$, $\Delta T^* = 0.2$), and (bottom) the coarse spatiotemporal resolution ($\Delta X^* = 8$, $\Delta T^* = 0.4$).

### 2) SENSITIVITY STUDY

A parametric study is conducted by varying $\Delta X^* = [2; 4; 8; 16]$ and $\Delta T^*$ for all advection schemes. For the four spatial resolutions, the gravity current is initially simulated

with the dimensionalized time step $\Delta t = 0.15$ s and then the complete simulation is reproduced by doubling the previous time step as long as the numerical stability is respected. The graphs in Fig. 8 represent integrated variables $\Sigma ||\mathbf{u}||^2$ and $\Sigma ||\boldsymbol{\omega}||^2$, which are nondimensionalized by the

TABLE 3. The impact of resolution: comparison of local and integrated variables. The REF0 reference simulation corresponds to the spatiotemporal resolution ($\Delta X^* = 1$, $\Delta T^* = 0.15$); the fine (coarse) resolution to [$\Delta X^* = 2$, $\Delta T^* = 0.2$ ($\Delta X^* = 8$, $\Delta T^* = 0.4$)]. Boldface characters indicate the results giving the lowest relative error compared to REF0.

| Advection | $\Delta\theta_{min}$ (K) | $u_{min}$ (m s$^{-1}$) | $u_{max}$ (m s$^{-1}$) | $v_{min}$ (m s$^{-1}$) | $U_{max}$ (m s$^{-1}$) | $x_{front}$ (km) | $\omega_{max}$ ($10^{-2}$ s$^{-1}$) | $2E_k$ (m$^2$ s$^{-2}$) | $E_s$ ($10^{-5}$ s$^{-2}$) |
|---|---|---|---|---|---|---|---|---|---|
| Scheme | | | | | | | | | |
| REF0 | −9.66 | −15.26 | 36.14 | −15.91 | 12.93 | 15.39 | 7.45 | 10.50 | 8.15 |
| Fine resolution | | | | | | | | | |
| WENO5 | **−9.72** | **−15.23** | **36.39** | **−15.97** | **12.98** | 15.31 | 7.38 | 10.42 | **8.07** |
| WENO3 | −9.60 | **−15.25** | 35.41 | −16.02 | 12.80 | 15.32 | 7.42 | 10.43 | 7.90 |
| CEN4TH | **−9.66** | **−15.24** | **36.11** | **−15.88** | **12.89** | **15.38** | **7.43** | **10.50** | **8.09** |
| Coarse resolution | | | | | | | | | |
| WENO5 | **−9.04** | **−14.04** | 32.53 | **−14.74** | 12.39 | 14.61 | **6.21** | **9.82** | **5.77** |
| WENO3 | −8.22 | −13.35 | 27.42 | −12.56 | 11.54 | 14.62 | 4.50 | 8.78 | 4.51 |
| CEN4TH | **−8.83** | −13.59 | **32.87** | −13.92 | 11.53 | **15.08** | 5.78 | **9.84** | 5.78 |
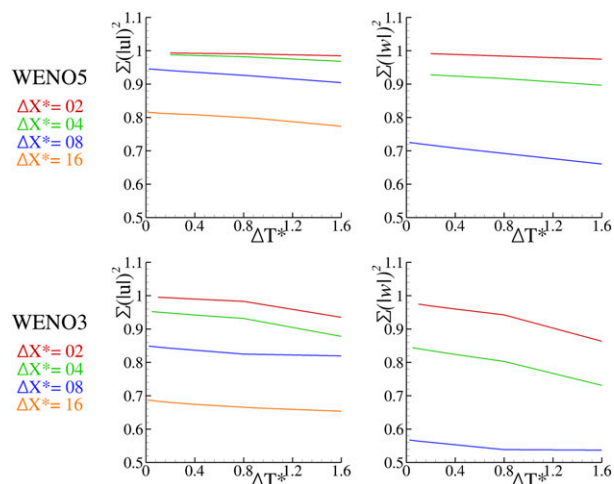
FIG. 8. Evolution at $t = 900$ s of the nondimensional $\Sigma\|\mathbf{u}\|^2$ and $\Sigma\|\boldsymbol{\omega}\|^2$ variables according to the time step $\Delta T^*$ and depending on the advection scheme (WENO3 and WENO5) for $\Delta X^* = 02$ (red), 04 (green), 08 (blue), and 16 (orange).

reference value obtained with REFO ($\Sigma\|\mathbf{u}\|^2 \rightarrow 1$ and $\Sigma\|\boldsymbol{\omega}\|^2 \rightarrow 1$ are expected). The abscissa corresponds to $\Delta T^*$ and the color code to $\Delta X^*$ ($\Delta X^* = 2$ in red, 4 in green, 8 in blue, and 16 in orange). Note that the $\Delta X^* = 16$ curves may not appear because of their relative error being larger than 50%. WENO simulations remain stable throughout the [0: 1.6] CFL range (note that the CEN4TH becomes unstable for CFL $> 0.5$). No clear dependency of the temporal stability threshold on $\Delta X^*$ is observed (CFL $> 1.6$ in all cases). The slope and the height of each curve provide information about the loss of energy. For a fixed-time resolution, WENO5 exhibits the best results on $\Sigma\|\mathbf{u}\|^2$ and $\Sigma\|\boldsymbol{\omega}\|^2$. For a fixed space resolution, the decrease of $\Sigma\|\mathbf{u}\|^2$ and $\Sigma\|\boldsymbol{\omega}\|^2$ with $\Delta T^*$ is greatest with WENO3. This slope can be related to the time order of the temporal algorithm (e.g., RK21 or RK53). Some combinations of WENO5–RK53 and WENO3–RK21 report that the slope value and the stability threshold increase with the algorithm order [$\Delta T^*_{\max}$(WENO5 − RK21) ≈ 2.4 and $\Delta T^*_{\max}$(WENO5 − RK53) ≈ 3.2; not illustrated here]. Additional tests on the activation or not of the time-splitting method show that it does not affect the threshold but improves the precision of the results when the chosen time step approaches the threshold (not illustrated here).

### 3) CONCLUSIONS

To conclude on the density current test case, Meso-NH shows good agreement with previous results, particularly in its ability to recover the converged solution with a weak dependence on the three momentum advection schemes. However, the parametric study in time and space reveals that WENO5 and CEN4TH propose the lowest degradation of the

numerical accuracy with the coarsest resolution. WENO5 has the advantage in the modeling of the rear rotor (conservative behavior) whereas CEN4TH shows the best ability to maintain the production of enstrophy at the head front (nonsmoothing behavior). The WENO5 results are less time dependent than those of WENO3. This release is partly due to the association of WENO5 with a higher-order RK algorithm. The higher CFL compensates for the higher computational costs of the WENO5 computations and of the RK steps. The assessment will now turn to test cases including physics.

### c. Large eddy simulation of fog

Particular attention is paid to LESs of clouds, first because LES is an important issue for models like Meso-NH, and second because advection plays the primary role in LES as most of the eddies are resolved. Therefore, cloud processes in LES require an accurate representation of transport, not only for water species. This can also be related to the cloud edge problem widely studied since Klaassen and Clark (1985) (e.g., Baba and Takahashi 2013). The advection scheme has to capture the cloud edge sharply, simulating its buoyancy without numerical diffusion. It will be shown here that this constraint is not restricted to the scalar advection scheme but also concerns the wind advection scheme. The simulation consists of an LES of radiation fog, performed over the Site Instrumental de Recherche par Télédétection Atmosphérique (SIRTA) observatory in the suburbs of Paris, France, which is dedicated to fog life cycle observation. The objective is to compare the impacts of the different advection schemes on the fog life cycle. The fog event studied took place on 15 November 2011 within the context of the ParisFog field campaign (Stolaki et al. 2015) and appeared at 0200 UTC. The site features open, flat, grassy ground, with a tree barrier 15 m high and 100 m wide on one side of the site and, for the case in question, the flow passes through this high tree barrier. Meso-NH is run at 5-m resolution over a horizontal domain of 1 km × 1 km. The physical parameterizations are a 1.5-order closure turbulent scheme from Cuxart et al. (2000) in 3D mode, a two-moment warm microphysical scheme based on Khairoutdinov and Kogan's (2000) work designed for LES studies (Geoffroy et al. 2008), and surface schemes from Masson et al. (2013). To take the impact of trees into account, drag terms have been added to the momentum and subgrid turbulent kinetic energy equations by Aumond et al. (2013). The model is initialized at 2320 UTC 14 November 2011 from the radiosonde launched by Météo-France in Trappes, located 15 km west of SIRTA. The time step is 0.1 s for the WENO and
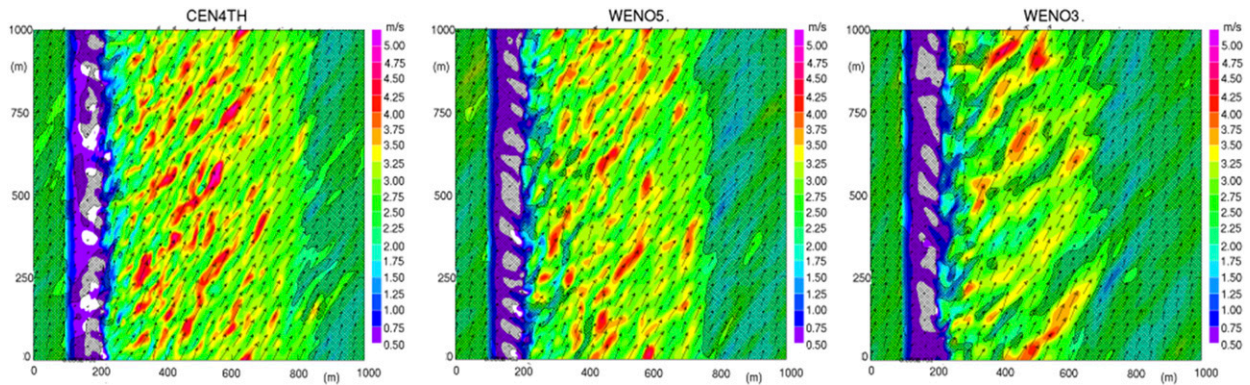
FIG. 9. LES FOG simulation: 10-m wind speed (m s$^{-1}$) with wind arrows and 10-m cloud mixing ratio $> 0.001$ g kg$^{-1}$ (shaded area) after 3 h of simulation.

CEN4TH schemes, even though WENO schemes allow a time step 10 times higher. The temporal scheme is RK53 for both WENO3 and WENO5 (with the addition of two time-splitting steps). The CEN4TH simulation uses the fourth-order diffusion scheme to suppress very short-wavelength modes, with an equivalent damping scale of 200 s for the $2\Delta x$ waves [noted $T_4(2)$ in appendix B].

Figure 9 illustrates the resolved turbulent structures induced by the tree barrier on the wind field after 3 h of simulations, aligned in the wind direction. As a result of this large resolved turbulence induced by trees, the impact of the different advection schemes is significant at the spatial scale of these coherent structures with finer and more numerous structures given by the CEN4TH simulation followed by WENO5; structures are coarser with WENO3. This is striking on the mean kinetic energy spectra applied to the vertical wind component, computed according to Ricard et al. (2013), which reveals effective resolutions of $4\Delta x$, $7 - 8\Delta x$, and $10 - 12\Delta x$ for CEN4TH, WENO5, and WENO3, respectively (Fig. 10 plotted during the mature stage of the fog life cycle). These differences among the dynamics directly impact the fog formation. Because of the subsidence downstream of the trees, CEN4TH and WENO5 tend to bring more of the warmer air from above and limit the formation of fog, compared to WENO3. The comparison of liquid water path (LWP) with the observations, which presents an error of up to 20 g m$^{-2}$ according to Löhnert and Crewell (2003), shows better agreement between CEN4TH and WENO5 than with WENO3 (which overestimates the cloud water amount). The observed LWP lies between the CEN4TH and WENO5 solutions (Fig. 11).

It can be added that, if the tree barrier is not taken into account in the model, the three advection schemes produce approximately the same simulation, with homogeneous fog over the area, appearing too early and

producing far too great a cloud water path, as a result of the cooling being too strong at the surface (not shown).

Thus, in this LES of fog, it appears that WENO5 is in good agreement with the observations and behaves similarly to CEN4TH, even if the effective resolution is coarser. It brings a significant improvement compared to WENO3, not only in terms of effective resolution, but also on the strength of the top entrainment process, which is crucial during the fog life cycle. This result also applies to other stratocumulus diurnal cycle simulations, for which WENO3 limits cloud-top entrainment and increases LWP. In terms of efficiency, the time step with WENO5 could be 10 times larger than with CEN4TH. In that case, because of the sub–time steps for wind and scalar advections, and to the more expensive algorithm of WENO5, the computational cost and the time to solution would be about 4 times less for WENO5 than for CEN4TH.

### d. The windstorm Klaus

The last study concerns a windstorm, for which the choice of wind advection scheme is expected to have an impact. The different advection schemes are compared on the European windstorm Klaus, which made landfall over large parts of central and southern France, Spain, and parts of Italy in January 2009. It caused 26 fatalities, as well as extensive disruptions to public transport and power supplies. The storm was the most damaging in France since Lothar and Martin in December 1999. Peak gusts reached more than 200 km h$^{-1}$, and sustained winds of more than 170 km h$^{-1}$ (hurricane-force winds) were observed. Klaus started on 23 January 2009 at about 0000 UTC in the middle of the Atlantic with a minimum MSLP value of 1000 hPa, according to ECMWF analysis. The track of the cyclone was in the zonal direction and its speed was remarkably high, reaching rates above 100 km h$^{-1}$. A minimum surface pressure of about 964 hPa at the cyclone's center occurred on day 24 at about
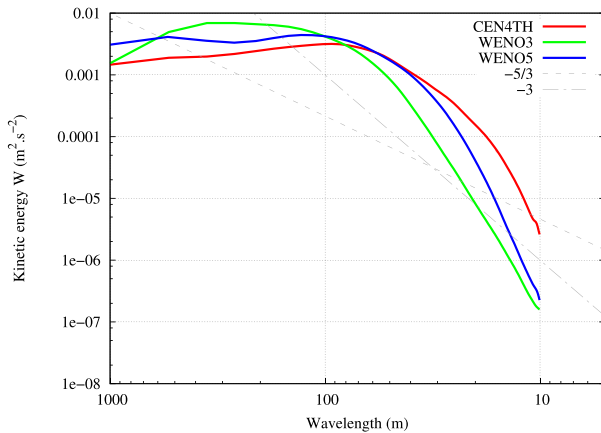
FIG. 10. Mean kinetic energy spectra for the vertical wind computed in the fog after 5 h of simulation: CEN4TH (red), WENO3 (green), and WENO5 (blue). The −5/3 (dashed) and −3 (dashed dot) lines are also shown.



FIG. 11. Time evolution of the liquid water path $(g\,kg^{-1})$ observed (black) and simulated with the CEN4TH (red), WENO3 (green), and WENO5 (blue) schemes.

0000 UTC. The storm made landfall near Bordeaux, France, at 0500 UTC 24 January, and traveled southeastward throughout the morning, finally reaching the southeast coast of France at 1300 UTC. It continued eastward over Italy, without causing significant damage.

Meso-NH is used in a configuration similar to the operational model AROME (Seity et al. 2011), at 2.5-km horizontal resolution over France, and with 46 vertical levels below 20 km. Simulations start from 0000 UTC 24 January 2009 with AROME or the ECMWF analysis, last 24 h, and are coupled with analysis every 3 h. AROME itself is coupled with the ARPEGE global model. The time step for Meso-NH is 60 s for simulations using the WENO schemes and 6 s for those using CEN4TH. The temporal scheme is RK53 for both WENO3 and WENO5, with two additional time-splitting steps. This means that the physics is called every 60 s for the WENO schemes, and every 6 s for CEN4TH. For CEN4TH, the equivalent damping scale of the numerical diffusion $[T_4(2)$ in B6] is 30 min. The physical package includes a mixed one-moment microphysical scheme (Pinty and Jabouille 1998), the 1.5-order closure turbulent scheme of Cuxart et al. (2000) in 1D mode, and the mass flux scheme of Pergaud et al. (2009) to parameterize the thermals of the convective boundary layer. Furthermore, it was checked that the differences in the time steps between the simulations were not the source of the discrepancies.

Figure 12 illustrates the 10-m mean wind speed simulated with CEN4TH at 0800 UTC over the whole domain, with observations superimposed, using either the ECMWF or AROME initial and coupling fields. The differences in the surface winds linked to initial and coupling conditions are significant, especially over the
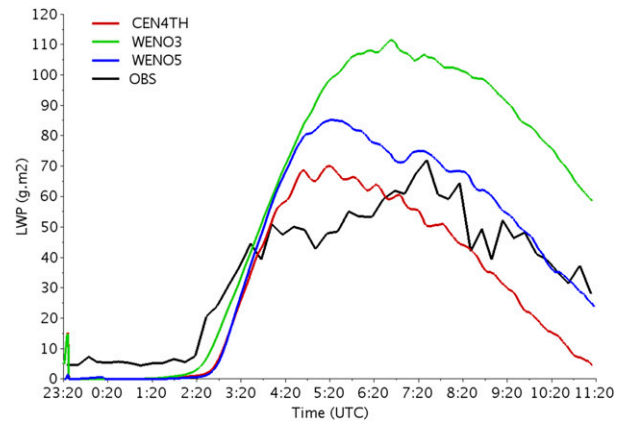
sea: ECMWF develops stronger winds over the Atlantic, which concerns the coastal areas. Some differences also appear over the continent across the west-northwest of France but for moderate winds.

Focusing on the southwestern region (Fig. 13), where the strongest winds occurred, the impact of the different advection schemes is seen to be weaker than the impact of the initial–coupling conditions. Biases and root-mean-square errors (RMSEs) are presented in Table 4 and Fig. 14 for every hour, over the whole domain of simulation (700 stations) or over southwest France (180 stations). First, two groups can be distinguished, depending on the coupled model. Considering ECMWF for the initial and coupling conditions, CEN4TH tends to develop the strongest winds, inducing a higher bias, in contrast to WENO3, which tends to smooth the wind field and to reduce the bias, as the winds are slightly too high with the ECMWF initial and coupling fields. But differences in bias and RMSE between CEN4TH and WENO3 do not exceed $0.5\,m\,s^{-1}$, with WENO5 presenting intermediate results. When using AROME as the initial–coupling conditions, the biases are sometimes positive and sometimes negative, but the RMSE is always higher than with the ECMWF initialization. None of the advection schemes has scores that are markedly better than the others. However, WENO3 has a small advantage as its smoother behavior tends to avoid the "double penalty" problem (Amodei and Stein 2009) where, first, the observation network is too sparse to easily validate all the wind scales present in the simulation and, second, the structures of the high-resolution fields can be spatially or temporally displaced.

Kinetic energy spectra can be applied to the zonal wind component (Fig. 15) for each Meso-NH simulation. They are presented for 0800 UTC as they were very similar for all times. Spectra for all the simulations
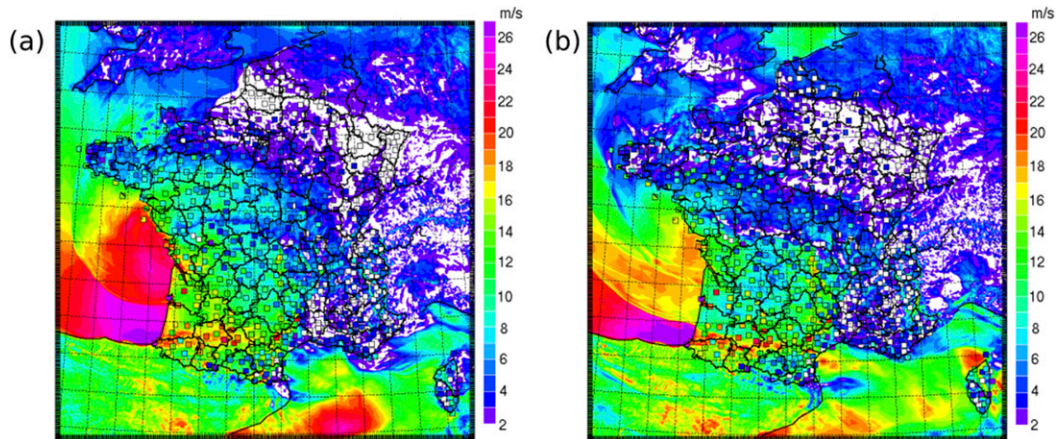
FIG. 12. Klaus simulation: 10-m wind speed (colored shading, m s$^{-1}$) simulated with CEN4TH, initialized and coupled with (a) ECMWF and (b) AROME analyses, with observations shown by the very small squares colored using the same legend, for 0800 UTC 24 Jan 2009 (averaged over the previous 10 min) over the whole domain.

match the $k^{-5/3}$ results well. In agreement with the previous LES study, the smallest diffusion in the shortest wavelengths is given by CEN4TH, followed by WENO5, and then WENO3. The most striking feature is that the gap between the three spectra occurs at large scale, up to 60 km, meaning that advection schemes impact not only the finest scales, but a significant part of the range of resolved scales. WENO5 presents a significant improvement compared to WENO3, and its behavior is intermediate between CEN4TH and WENO3. The gap between the CEN4TH and WENO5 spectra only increases below $3 - 4\Delta x$, while the CEN4TH spectrum is slightly impacted by the $2\Delta x$ waves, indicating that the numerical diffusion (applied only with CEN4TH) could be slightly increased. As in Ricard et al. (2013), Meso-NH spectra can be compared to the AROME forecast spectrum, as the initial conditions are the same (AROME analysis) as well as the physics. Only the dynamical core and the coupling fields (ARPEGE forecast for AROME and AROME analysis for Meso-NH) are different. In agreement with Ricard et al. (2013), the AROME forecast presents a higher diffusion toward the finescale, probably as a result of the implicit diffusion of the semi-implicit semi-Lagrangian (SISL) scheme. The AROME and WENO3 spectra are similar up to $5\Delta x$. The AROME forecast loses variance compared to WENO3 between $4\Delta x$ and $3\Delta x$ and at $3\Delta x$ as a result of an additional spectral quadratic truncation.

In terms of computational time, for the same frequency of call to the physics, CEN4TH would be cheaper, followed by WENO3 and then WENO5. For the simulations of the windstorm, the physics package was applied after each dynamics update, and produced a simulation time for WENO5 (WENO3) that was 38% (27%) of CEN4TH. Explicitly, for the

24 h of simulation, the computational costs were 120 h for the CEN4TH simulation, 45 h for WENO5, and 32 h for WENO3.

To conclude on this windstorm case, the strongest sensitivity to the Meso-NH results is seen in the initial and coupling fields. Nevertheless, the choice of advection scheme impacts the surface wind scores without permitting the best one to be determined. The smoother behavior of WENO3 tends to avoid the double-penalty problem and to score better, but it removes the kinetic energy variance at fairly large scales. However, below $5\Delta x$ of the spatial scale, WENO3 is less diffusive than the SISL scheme of AROME. WENO5's behavior is intermediate between WENO3 and CEN4TH in terms of scores and energy spectra. These conclusions, drawn from the windstorm case, are representative of most of the real-case simulations at the mesoscale.

## 4. Conclusions

This multi-test study has provided a complete overview of the different combinations of WENO momentum transport schemes (third and fifth order) with ERK temporal methods in terms of stability and accuracy with Meso-NH. The linear theoretical von Neumann analysis, expanded with a new graphical method, revealed that WENO3 with forward Euler and WENO5 with forward Euler and the second-order RK method were linearly unstable, as already shown by Wang and Spiteri (2007). RK53, RKC4, and, to a lesser degree, RK33 were the most efficient methods with WENO schemes (larger CFL numbers). The hydrostatic mountain wave test completed the stability study in 2D mode. The five-stage third- and fourth-order ERK
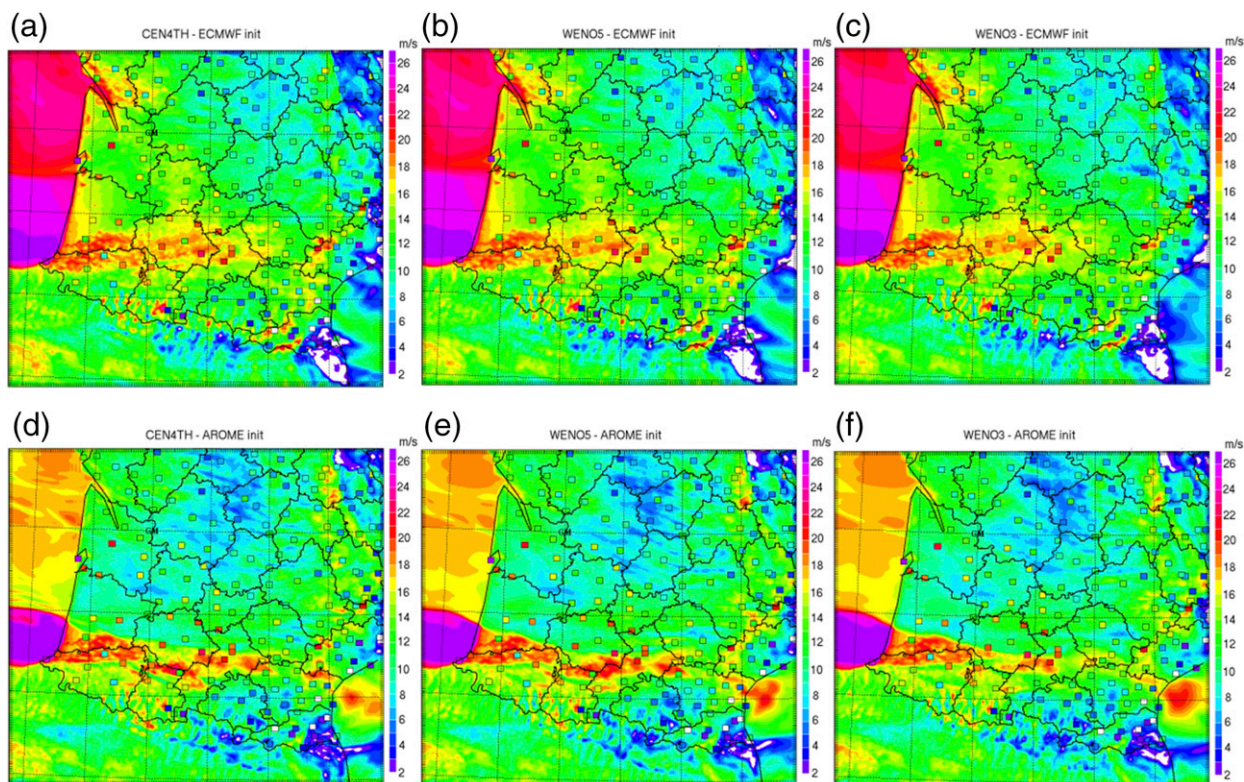
FIG. 13. Klaus simulation: 10-m simulated wind speed (colored shading, m s$^{-1}$) for 0800 UTC 24 Jan 2009 (averaged over the previous 10 min) zoomed-in over southwestern France, initialized and coupled with (top) the ECMWF and (bottom) AROME analyses with observations shown by very small squares colored using the same legend: (a),(d) CEN4TH, (b),(e) WENO5, and (c),(f) WENO3 schemes.

methods have been selected as optimal choices considering the maximum allowed time step and memory storage. WENO5 combined with RK53 presented a small time-step dependency on the cold-bubble test case. Furthermore, an additional time splitting of the ERK temporal discretization was very beneficial to the stability, allowing CFL numbers of 1.8 to be reached for WENO5 and 2.5 for WENO3, with an optimal sub-time-step number of 2. This method is of great interest for complete Meso-NH runs, as it limits the number of calls to the rest of the model (physics and pressure solver mainly).

The stability analysis has been complemented by an evaluation of the WENO schemes, with the fourth-order centered scheme associated with the leapfrog scheme as a basis for reference. WENO5 presents low-diffusion properties in the area of sharp gradients, whereas this is partly hidden with WENO3 because of its strong diffusive character relative to its lower order. These properties have been pointed out on the density current test case, where WENO5 accurately reproduced the rear rotor; and at the top of the fog layer in the LES, where the overdiffusive WENO3 scheme reduced the top entrainment

process, modifying the amount of cloud water and the fog life cycle.

In terms of accuracy, which is the first asset of the fourth-order centered scheme as already shown by

TABLE 4. Bias and RMSE scores (m s$^{-1}$) of 10-m wind speed (averaged over 10 min before each hour) over the whole domain of France and over the southwestern part with the different advection schemes and with AROME or ECMWF initialization and coupling.

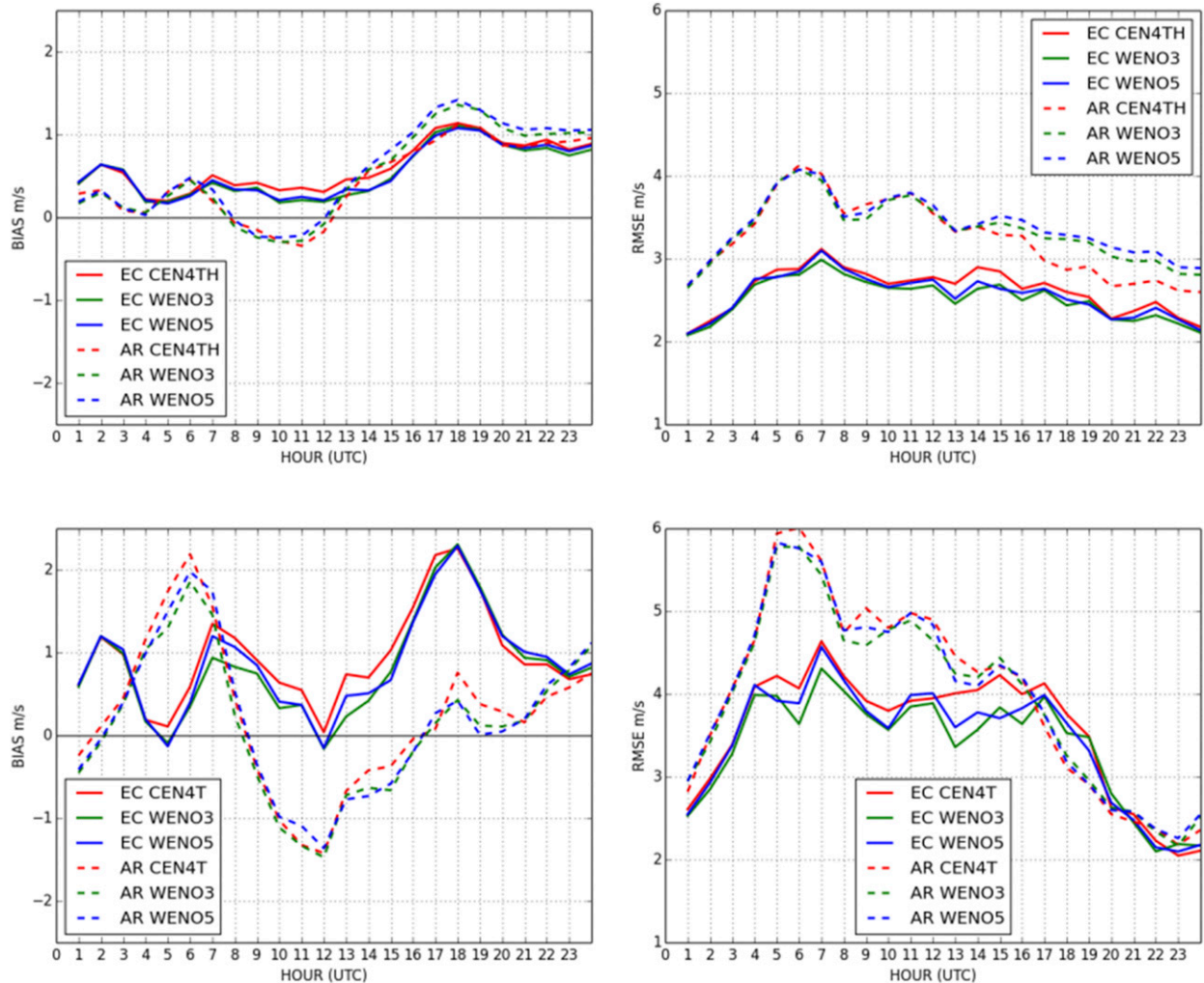| France | | | |
|---|---|---|---|
| | CEN4TH | WENO5 | WENO3 |
| **AROME initialization** | | | |
| Bias | 0.44 | 0.55 | 0.51 |
| RMSE | 3.28 | 3.41 | 3.36 |
| **ECMWF initialization** | | | |
| Bias | 0.61 | 0.55 | 0.54 |
| RMSE | 2.63 | 2.57 | 2.53 |
| Southwestern France | | | |
| | CEN4TH | WENO5 | WENO3 |
| **AROME initialization** | | | |
| Bias | 0.22 | 0.17 | 0.11 |
| RMSE | 4.17 | 4.14 | 4.10 |
| **ECMWF initialization** | | | |
| Bias | 0.94 | 0.86 | 0.82 |
| RMSE | 3.63 | 3.51 | 3.43 |

FIG. 14. Klaus simulation: time evolution on 24 Jan 2009 of the mean (left) BIAS and (right) RMSE deviation between the simulation and observations of 10-m wind speed (averaged over 10 min before each hour) over (top) the whole domain and (bottom) southwestern France. Simulations are initialized and coupled with ECMWF (noted EC) or AROME (noted AR): EC CEN4TH (solid red), EC WENO3 (solid green), EC WENO5 (solid blue), AR CEN4TH (dashed red), AR WENO3 (dashed green), and AR WENO5 (dashed blue).

Ricard et al. (2013), WENO5 is somewhat less attractive than CEN4TH, but presents fairly good abilities with an effective resolution of $7 - 8\Delta x$ on the fog LES and windstorm cases (compared to the $4\Delta x$ for CEN4TH and $10 - 12\Delta x$ for WENO3).

Thanks to the ERK method and the additional time splitting, and despite the more expensive spatial algorithm, the reduction of the computational cost of the Meso-NH runs is significant when the WENO schemes are implemented, with a mean factor of 3 for WENO5 and 4 for WENO3 compared to the fourth-order centered scheme, where the whole model, including the physics, is called. This improvement is very useful for the Meso-NH model, within the context of the widespread use of LES on large grids (Bergot et al. 2015; Dauhut et al. 2015). The benefit is

still more significant for aerosol and chemistry runs, as the expensive chemistry is called with large time steps.

Thus, it has been shown that time discretization of wind gradient terms using ERK methods with an added time splitting step can bring considerable benefit in terms of the stability and time dependence of the solution. In further work, it would be interesting to evaluate these time integration methods and also Kinnmark and Gray's (1984) methods with the CEN4TH space discretization in order to keep its accuracy and to reach higher CFL numbers.
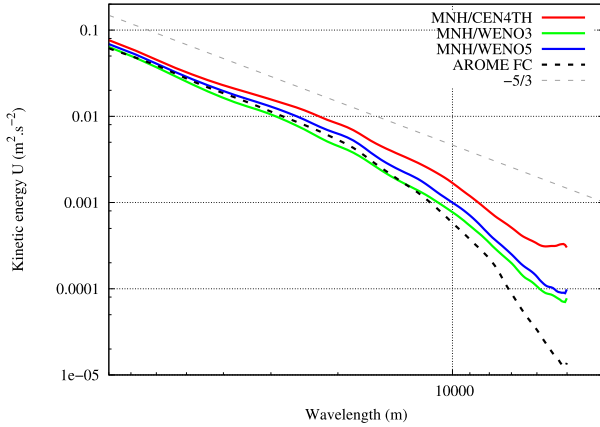
FIG. 15. Klaus simulation: mean kinetic energy spectra for zonal wind computed at 0800 UTC 24 Jan 2009 over the whole domain, applied to Meso-NH simulations, initialized and coupled with AROME analysis, with the different schemes and applied to AROME forecasts (denoted AROME FC, dashed black): CEN4TH (red), WENO3 (green), and WENO5 (blue). The −5/3 profile is shown as a gray dashed line.

for his helpful remarks and Pierre Lassègues for providing observations of the Klaus windstorm.

## APPENDIX A

### WENO Stencil Definition

The WENO5 stencils are given by

$$\gamma_j = \frac{\alpha_j}{\alpha_0 + \alpha_1 + \alpha_2}, \quad (A1)$$

where the nonnormalized stencil weights are

$$\alpha_0 = \frac{1}{10}\left(\frac{1}{\varepsilon + \beta_0}\right)^2, \quad \alpha_1 = \frac{6}{10}\left(\frac{1}{\varepsilon + \beta_1}\right)^2,$$
$$\alpha_2 = \frac{3}{10}\left(\frac{1}{\varepsilon + \beta_2}\right)^2. \quad (A2)$$

The $\varepsilon$ term is used here to prevent the denominator from being null and is set to $10^{-15}$ in the model. The $\beta_j$ terms, also called indicators of smoothness, are the heart of the ENO methods, of which WENO schemes are extensions. They are defined below:

$$\beta_0 = \frac{13}{12}(\overline{u}_{i-2} - 2\overline{u}_{i-1} + \overline{u}_i)^2 + \frac{1}{4}(\overline{u}_{i-2} - 4\overline{u}_{i-1} + 3\overline{u}_i)^2,$$
$$\beta_1 = \frac{13}{12}(\overline{u}_{i-1} - 2\overline{u}_i + \overline{u}_{i+1})^2 + \frac{1}{4}(\overline{u}_{i-1} - \overline{u}_{i+1})^2, \quad \text{and}$$
$$(A3)$$
$$\beta_2 = \frac{13}{12}(\overline{u}_i - 2\overline{u}_{i+1} + \overline{u}_{i+2})^2 + \frac{1}{4}(3\overline{u}_i - 4\overline{u}_{i+1} + \overline{u}_{i+2})^2.$$

WENO5 reverts to WENO3 at the edges of the computational domain for open boundary conditions only. The WENO3 stencils are given by

$$\gamma_j = \frac{\alpha_i}{\alpha_0 + \alpha_1}, \quad (A4)$$

where the nonnormalized stencil weights are

$$\alpha_0 = \frac{1}{3}\left(\frac{1}{\varepsilon + \beta_0}\right)^2, \quad \alpha_1 = \frac{2}{3}\left(\frac{1}{\varepsilon + \beta_1}\right)^2, \quad (A5)$$

and for the smoothness indicators,

$$\beta_0 = (-\overline{u}_{i-1} + \overline{u}_i)^2, \quad \beta_1 = (-\overline{u}_i + \overline{u}_{i+1})^2. \quad (A6)$$

## APPENDIX B

### Numerical Diffusion Operator

The diffusion operator applied to the momentum components $\phi$ is a fourth-order operator used everywhere except at the first interior grid point where a second operator is substituted in the case of nonperiodic boundary conditions. It reads

$$D_\phi = -K_4\left(\frac{\partial^4\phi}{\partial x^4} + \frac{\partial^4\phi}{\partial y^4}\right), \quad (B1)$$

where $K_4$ is the positive diffusion coefficient, with the fourth derivative needing a minus sign to damp waves. The second-order accurate discretization is

$$\left(\frac{\partial^4\phi}{\partial x^4}\right)_i \sim \frac{6\phi_i - 4(\phi_{i+1} + \phi_{i-1}) + (\phi_{i+2} + \phi_{i-2})}{\Delta x^4}, \quad (B2)$$

where $\Delta x$ and $i$ are the grid increment and the spatial index, respectively. Considering a single harmonic wave defined by $\phi(x, t) = \Phi(t)e^{ikx}$, where $\Phi(t)$ is the wave amplitude and $k$ the wavenumber, the application of a fourth-order diffusion operator during $N$ time steps leads to

$$\phi(x, t + N\Delta t) = \Phi(t)\left[1 - 4\frac{K_4\Delta t}{\Delta x^4}(1 - \cos k\Delta x)^2\right]^N. \quad (B3)$$

The time $T_4$ at which the initial wave is damped by $e^{-1}$ is then

$$T_4 = N\Delta t = \frac{-\Delta t}{\ln\left[1 - 4\frac{K_4\Delta t}{\Delta x^4}(1 - \cos k\Delta x)^2\right]}, \quad (B4)$$

which can be approximated by

$$T_4 \sim \frac{\Delta x^4}{4K_4(1 - \cos k\Delta x)^2}. \tag{B5}$$

If $k$ is the wavenumber associated with the $n\Delta x$ wavelength, $T_4$ is given by

$$T_4(n) \sim \frac{\Delta x^4}{4K_4(1 - \cos 2\pi/n)^2}. \tag{B6}$$

As it is more convenient to specify $T_4$, for a given simulation, we fix $T_4(2)$ as the equivalent damping time scale for the $2\Delta x$ waves.

## APPENDIX C

### Fourier Symbols of WENO Schemes

The Fourier symbol of the fifth-order WENO method can be written for smooth solutions as

$$z_{\text{WENO5}}(\theta_\kappa) = \frac{-2e^{-3i\theta_\kappa} + 15e^{-2i\theta_\kappa} - 60e^{-i\theta_\kappa}}{60}$$
$$+ \frac{20 + 30e^{i\theta_\kappa} - 3e^{2i\theta_\kappa}}{60}. \tag{C1}$$

This is the same formula as is used for the upwind form of fifth order given by Baldauf (2008). When smooth solutions are considered, the indicators of smoothness $\beta_i$ are close to one, so the flux reconstruction can be approximated to the upwind form of the same order, as in Motamed et al. (2011).

The Fourier symbol of the third-order WENO method can be similarly written for smooth solutions:

$$z_{\text{WENO3}}(\theta_\kappa) = \frac{e^{-2i\theta_\kappa} - 6e^{-i\theta_\kappa} + 3 + 2e^{i\theta_\kappa}}{6}. \tag{C2}$$

## APPENDIX D

### Explicit Runge–Kutta Methods

#### a. General description of a Runge–Kutta method

To integrate the ordinary differential equation

$$\frac{du}{dt} = f(u, t)$$

between $t_n$ and $t_{n+1}$, the ERK method uses $s$ intermediate steps as follow:

$$k_1 = f(t_n, u^n)$$
$$k_2 = f[t_n + c_2\Delta t, u^n + \Delta t(a_{21}k_1)]$$
$$k_3 = f[t_n + c_3\Delta t, u^n + \Delta t(a_{31}k_1 + a_{32}k_2)]$$
$$\vdots$$
$$k_s = f[t_n + c_s\Delta t, u^n + \Delta t(a_{s1}k_1 + a_{s2}k_2 + \cdots + a_{s,s-1}k_{s-1})].$$

Then, the final solution at $t_{n+1}$ is obtained by

$$u^{n+1} = u^n + \Delta t \sum_{i=1}^{s} b_i k_i. \tag{D1}$$

Note that the $c_i$ coefficients are not used when integrating the Euler equations, because there is no time-dependent term in the operator $f$.

#### b. Butcher tables

Several methods are represented in the following tables, with their Butcher coefficients. First, some well-known classical methods from the literature are presented:

forward Euler (FF),

$$\begin{array}{c|c} 0 & \\ \hline & 1 \end{array};$$

Heun (HEUN2),

$$\begin{array}{c|cc} 0 & & \\ 1 & 1 & \\ \hline & 1/2 & 1/2 \end{array}; \quad \text{and}$$

ERK order 4 (RKC4),

$$\begin{array}{c|cccc} 0 & & & & \\ 1/2 & 1/2 & & & \\ & 0 & 1/2 & & \\ 1 & 0 & 0 & 1 & \\ \hline & 1/6 & 1/3 & 1/3 & 1/6 \end{array}.$$

Other methods from Wang and Spiteri (2007) are presented below:

ERK with order 1 and two steps (RK21),

$$\begin{array}{c|cc} 0 & & \\ 3/4 & 3/4 & \\ \hline & 0 & 1 \end{array};$$

SSP-RK with order 3 and three steps (RK33),

$$
\begin{array}{c|ccc}
0 & & & \\
1 & 1 & & \\
1/2 & 1/4 & 1/4 & \\
\hline
& 1/6 & 1/6 & 2/3
\end{array}
\quad ; \quad \text{and}
$$

ERK with order 3 and five steps (RK53),

$$
\begin{array}{c|ccccc}
0 & & & & & \\
1/7 & 1/7 & & & & \\
3/16 & 0 & 3/16 & & & \\
1/3 & 0 & 0 & 1/3 & & \\
2/3 & 0 & 0 & 0 & 2/3 & \\
\hline
& 1/4 & 0 & 0 & 0 & 3/4
\end{array}
\quad .
$$

## APPENDIX E

### Reference Solution of the Cold-Bubble Test

To study the spatiotemporal resolution on the gravity current case (Straka et al. (1993)), here, we compare the Meso-NH (MNH) results on a converged solution with the literature: the EULAG anelastic nonhydrostatic model in Rosa et al. (2011), the discontinuous Galerkin evolution model (DGEM) in Müller et al. (2013), the fully compressible reference solution (REFC) obtained by Straka et al. (1993), the fully compressible WRF Model in Skamarock and Klemp (2008), the anelastic nonhydrostatic ARPS model in Xue et al. (2000), and the SISL compressible nonhydrostatic model in Melvin et al. (2010).

When the time and spatial discretizations are sufficient to simulate a converged solution [the diffusion term defined by Straka et al. (1993) allows this], the solution has to be weakly dependent on the choice of the advection scheme. To obtain the reference solution, we use CEN4TH (leapfrog). Note that the first 300 s were simulated with WENO5 (RK53) to verify that the results were independent of the advection schemes. The mesh covers $2048 \times 256$ points ($x_{ref} = 25$ m) and fixes the time step at $\Delta t = 0.1$ s. Until $t = 900$ s, the density current undergoes a horizontal acceleration and a maximum is reached on the velocity magnitude at $t \approx 300$ s, so we define the characteristic velocity $||\mathbf{u}||_{max}$ as $||\mathbf{u}||_{max}$ (300 s) $\approx 40$ m s$^{-1}$. The CFL ($= ||\mathbf{u}||_{max} \Delta t / \Delta x$) is not violated and divided by at least 6.

Table E1 compares our result with those using the same spatial discretization [except for Müller et al. (2013), who used an adaptive mesh refinement (AMR) technique with an equivalent space step $\Delta x_{eff} = 28.26$ m]. The differences in $u_{min}$, $v_{min}$, and $v_{max}$ are in good agreement (EULAG/REFC/MNH). More discrepancies between the results appear in $u_{max}$ and seem to be related to

TABLE E1. The converged solution: comparison of local variables obtained by different models using $\Delta x_{ref} = 25$ m ($\Delta \theta$ in K, $\mathbf{u}$ in m s$^{-1}$, and $x_{front}$ in km).

| Model | $\Delta\theta_{min}$ | $u_{min}$ | $u_{max}$ | $v_{min}$ | $v_{max}$ | $x_{front}$ |
|---|---|---|---|---|---|---|
| EULAG | −9.96 | −15.29 | 35.06 | −15.94 | 13.07 | 15.16 |
| DEGM | −9.80 | | | | | 15.44 |
| REFC | −9.77 | −15.19 | 36.46 | −15.95 | 12.93 | 15.53 |
| WRF | −9.70 | | | | | 15.38 |
| ARPS | −9.68 | | | | | 15.40 |
| SISL | −9.66 | | | | | 15.39 |
| MNH | −9.66 | −15.26 | 36.14 | −15.91 | 12.93 | 15.39 |

the variation observed at the front location [defined by $x_{max}$ ($\Delta\theta = -1$ K]. Good agreement is observed for $\Delta\theta_{min}$ and $x_{front}$ for the WRF/SISL/ARPS/MNH codes. When the Richardson extrapolation performed by Straka et al. (1993) is added, suggesting a grid-converged solution with $\Delta x_{ref} = 25$ m, the reference simulation REFO can be considered to be validated.

## REFERENCES

Amodei, M., and J. Stein, 2009: Deterministic and fuzzy verification methods for a hierarchy of numerical models. *Meteor. Appl.*, **16**, 191–203, doi:10.1002/met.101.

Aranami, K., T. Davies, and N. Wood, 2015: A mass restoration scheme for limited-area models with semi-Lagrangian advection. *Quart. J. Roy. Meteor. Soc.*, **141**, 1795–1803, doi:10.1002/qj.2482.

Aumond, P., V. Masson, C. Lac, B. Gauvreau, S. Dupont, and M. Berengier, 2013: Including the drag effects of canopies: Real case large-eddy simulation studies. *Bound.-Layer Meteor.*, **146**, 65–80, doi:10.1007/s10546-012-9758-x.

Baba, Y., and K. Takahashi, 2013: Weighted essentially non-oscillatory scheme for cloud edge problem. *Quart. J. Roy. Meteor. Soc.*, **139**, 1374–1388, doi:10.1002/qj.2030.

Baldauf, M., 2008: Stability analysis for linear discretisations of the advection equation with Runge–Kutta time integration. *J. Comput. Phys.*, **227**, 6638–6659, doi:10.1016/j.jcp.2008.03.025.

——, A. Seifert, J. Förstner, D. Majewski, M. Raschendorfer, and T. Reinhardt, 2011: Operational convective-scale numerical weather prediction with the COSMO model: Description and sensitivities. *Mon. Wea. Rev.*, **139**, 3887–3905, doi:10.1175/MWR-D-10-05013.1.

Bergot, T., J. Escobar, and V. Masson, 2015: Effect of small-scale surface heterogeneities and buildings on radiation fog: Large-eddy simulation study at Paris Charles de Gaulle Airport. *Quart. J. Roy. Meteor. Soc.*, **141**, 285–298, doi:10.1002/qj.2358.

Carpenter, R. L., K. K. Droegemeier, P. R. Woodward, and C. E. Hane, 1990: Application of the piecewise parabolic method (PPM) to meteorological modeling. *Mon. Wea. Rev.*, **118**, 586–612, doi:10.1175/1520-0493(1990)118<0586:AOTPPM>2.0.CO;2.

Castro, M., B. Costa, and W. S. Don, 2011: High order weighted essentially non-oscillatory WENO-Z schemes for hyperbolic conservation laws. *J. Comput. Phys.*, **230**, 1766–1792, doi:10.1016/j.jcp.2010.11.028.

Chaudhuri, A., A. Hadjadj, and A. Chinnayya, 2011: On the use of immersed boundary methods for shock/obstacle interactions. *J. Comput. Phys.*, **230**, 1731–1748, doi:10.1016/j.jcp.2010.11.016.

Colella, P., and P. R. Woodward, 1984: The piecewise parabolic method (PPM) for gas-dynamical simulations. *J. Comput. Phys.*, **54**, 174–201, doi:10.1016/0021-9991(84)90143-8.

Crank, J., and P. Nicolson, 1947: A practical method for numerical evaluation of solutions of partial differential equations of the heat-conduction type. *Math. Proc. Cambridge Philos. Soc.*, **43**, 50–67.

Cuxart, J., P. Bougeault, and J.-L. Redelsperger, 2000: A turbulence scheme allowing for mesoscale and large-eddy simulations. *Quart. J. Roy. Meteor. Soc.*, **126**, 1–30, doi:10.1002/qj.49712656202.

Dauhut, T., J.-P. Chaboureau, J. Escobar, and P. Mascart, 2015: Large-eddy simulations of Hector the convector making the stratosphere wetter. *Atmos. Sci. Lett.*, **16**, 135–140, doi:10.1002/asl2.534.

Davies, T., M. Cullen, A. Malcolm, M. Mawson, A. Staniforth, A. White, and N. Wood, 2005: A new dynamical core for the Met Office's global and regional modelling of the atmosphere. *Quart. J. Roy. Meteor. Soc.*, **131**, 1759–1782, doi:10.1256/qj.04.101.

Durran, D. R., 1989: Improving the anelastic approximation. *J. Atmos. Sci.*, **46**, 1453–1461, doi:10.1175/1520-0469(1989)046<1453:ITAA>2.0.CO;2.

——, and J. B. Klemp, 1983: A compressible model for the simulation of moist mountain waves. *Mon. Wea. Rev.*, **111**, 2341–2361, doi:10.1175/1520-0493(1983)111<2341:ACMFTS>2.0.CO;2.

Erath, C., M. A. Taylor, and R. D. Nair, 2016: Two conservative multi-tracer efficient semi-Lagrangian schemes for multiple processor systems integrated in a spectral element (climate) dynamical core. *Commun. Appl. Indust. Math.*, **7**, 74–98, doi:10.1515/caim-2016-0023.

Feistauer, M., J. Felcman, and I. Straškraba, 2003: *Mathematical and Computational Methods for Compressible Flow.* Oxford University Press, 552 pp.

Gal-Chen, T., and R. C. Somerville, 1975: On the use of a coordinate transformation for the solution of the Navier–Stokes equations. *J. Comput. Phys.*, **17**, 209–228, doi:10.1016/0021-9991(75)90037-6.

Geoffroy, O., J.-L. Brenguier, and I. Sandu, 2008: Relationship between drizzle rate, liquid water path and droplet concentration at the scale of a stratocumulus cloud system. *Atmos. Chem. Phys.*, **8**, 4641–4654, doi:10.5194/acp-8-4641-2008.

Ghosal, S., 1996: An analysis of numerical errors in large-eddy simulations of turbulence. *J. Comput. Phys.*, **125**, 187–206, doi:10.1006/jcph.1996.0088.

Huang, B., D. Chen, X. Li, and C. Li, 2014: Improvement of the semi-Lagrangian advection scheme in the GRAPES model: Theoretical analysis and idealized tests. *Adv. Atmos. Sci.*, **31**, 693–704, doi:10.1007/s00376-013-3086-z.

Jiang, G.-S., and C.-W. Shu, 1995: Efficient implementation of weighted ENO schemes. *J. Comput. Phys.*, **126**, 202–228, doi:10.1006/jcph.1996.0130.

Khairoutdinov, M., and Y. Kogan, 2000: A new cloud physics parameterization in a large-eddy simulation model of marine stratocumulus. *Mon. Wea. Rev.*, **128**, 229–243, doi:10.1175/1520-0493(2000)128<0229:ANCPPI>2.0.CO;2.

Kinnmark, I. P. E., and W. Gray, 1984: One step integration methods of third-fourth order accuracy with large hyperbolic stability limits. *Math. Comput. Simul.*, **26**, 181–188, doi:10.1016/0378-4754(84)90056-9.

Klaassen, G. P. and T. L. Clark, 1985: Dynamics of the cloud-environment interface and entrainment in small cumuli: Two-dimensional simulations in the absence of ambient shear. *J. Atmos.*

*Sci.*, **42**, 2621–2642, doi:10.1175/1520-0469(1985)042<2621:DOTCEI>2.0.CO;2

Klemp, J. B., W. C. Skamarock, and O. Fuhrer, 2003: Numerical consistency of metric terms in terrain-following coordinates. *Mon. Wea. Rev.*, **131**, 1229–1239, doi:10.1175/1520-0493(2003)131<1229:NCOMTI>2.0.CO;2.

Kurowski, M. J., W. W. Grabowski, and P. K. Smolarkiewicz, 2014: Anelastic and compressible simulation of moist deep convection. *J. Atmos. Sci.*, **71**, 3767–3787, doi:10.1175/JAS-D-14-0017.1.

Lafore, J., J. Stein, N. Asencio, P. Bougeault, V. Ducrocq, J. Duron, and C. Fischer, 1998: The Meso-NH atmospheric simulation system. Part I: Adiabatic formulation and control simulations. *Ann. Geophys.*, **16**, 90–109, doi:10.1007/s00585-997-0090-6.

Lauritzen, P. H., M. A. Taylor, J. Overfelt, P. A. Ullrich, R. D. Nair, S. Goldhaber, and R. Kelly, 2017: CAM-SE–CSLAM: Consistent coupling of a conservative semi-Lagrangian finite-volume method with spectral element dynamics. *Mon. Wea. Rev.*, **145**, 833–855, doi:10.1175/MWR-D-16-0258.1.

Lipps, F. B., and R. S. Hemler, 1982: A scale analysis of deep moist convection and some related numerical calculations. *J. Atmos. Sci.*, **39**, 2192–2210, doi:10.1175/1520-0469(1982)039<2192:ASAODM>2.0.CO;2.

Löhnert, U., and S. Crewell, 2003: Accuracy of cloud liquid water path from ground-based microwave radiometry 1. Dependency on cloud model statistics. *Radio Sci.*, **38**, 8041, doi:10.1029/2002RS002654.

Masson, V., and Coauthors, 2013: The SURFEXv7. 2 land and ocean surface platform for coupled or offline simulation of earth surface variables and fluxes. *Geosci. Model Dev.*, **6**, 929–960, doi:10.5194/gmd-6-929-2013.

Melvin, T., M. Dubal, N. Wood, A. Staniforth, and M. Zerroukat, 2010: An inherently mass-conserving iterative semi-implicit semi-Lagrangian discretization of the non-hydrostatic vertical-slice equations. *Quart. J. Roy. Meteor. Soc.*, **136**, 799–814, doi:10.1002/qj.603.

Motamed, M., C. B. Macdonald, and S. J. Ruuth, 2011: On the linear stability of the fifth-order WENO discretization. *J. Sci. Comput.*, **47**, 127–149, doi:10.1007/s10915-010-9423-9.

Müller, A., J. Behrens, F. X. Giraldo, and V. Wirth, 2013: Comparison between adaptive and uniform discontinuous Galerkin simulations in dry 2D bubble experiments. *J. Comput. Phys.*, **235**, 371–393, doi:10.1016/j.jcp.2012.10.038.

Osher, S., and R. Fedkiw, 2003: *Level Set Methods and Dynamic Implicit Surfaces.* Applied Mathematical Sciences, Vol. 153, Springer-Verlag, 273 pp.

Pergaud, J., V. Masson, S. Malardel, and F. Couvreux, 2009: A parameterization of dry thermals and shallow cumuli for mesoscale numerical weather prediction. *Bound.-Layer Meteor.*, **132**, 83–106, doi:10.1007/s10546-009-9388-0.

Pinty, J.-P., and P. Jabouille, 1998: A mixed-phase cloud parameterization for use in mesoscale non-hydrostatic model: simulations of a squall line and of orographic precipitations. Preprints, *Conf. of Cloud Physics*, Everett, WA, Amer. Meteor. Soc., 217–220.

Pressel, K. G., C. M. Kaul, T. Schneider, Z. Tan, and S. Mishra, 2015: Large-eddy simulation in an anelastic framework with closed water and entropy balances. *J. Adv. Model. Earth Syst.*, **7**, 1425–1456, doi:10.1002/2015MS000496.

Ricard, D., C. Lac, S. Riette, R. Legrand, and A. Mary, 2013: Kinetic energy spectra characteristics of two convection-permitting

limited-area models AROME and Meso-NH. *Quart. J. Roy. Meteor. Soc.*, **139**, 1327–1341, doi:10.1002/qj.2025.

Rosa, B., M. Kurowski, and M. Ziemiański, 2011: Testing the anelastic nonhydrostatic model EULAG as a prospective dynamical core of a numerical weather prediction model. Part I: Dry benchmarks. *Acta Geophys.*, **59**, 1236–1266, doi:10.2478/s11600-011-0041-1.

Schär, C., D. Leuenberger, O. Fuhrer, D. Lüthi, and C. Girard, 2002: A new terrain-following vertical coordinate formulation for atmospheric prediction models. *Mon. Wea. Rev.*, **130**, 2459–2480, doi:10.1175/1520-0493(2002)130<2459:ANTFVC>2.0.CO;2.

Seity, Y., P. Brousseau, S. Malardel, G. Hello, P. Bénard, F. Bouttier, C. Lac, and V. Masson, 2011: The AROME-France convective-scale operational model. *Mon. Wea. Rev.*, **139**, 976–991, doi:10.1175/2010MWR3425.1.

Shashkin, V., R. Fadeev, and M. Tolstykh, 2016: 3D conservative cascade semi-Lagrangian transport scheme using reduced latitude–longitude grid (CCS-RG). *J. Comput. Phys.*, **305**, 700–721, doi:10.1016/j.jcp.2015.11.005.

Shu, C.-W., 1998: Essentially non-oscillatory and weighted essentially non-oscillatory schemes for hyperbolic conservation laws. *Advanced Numerical Approximation of Nonlinear Hyperbolic Equations*, A. Quarteroni, Ed., Lecture Notes in Mathematics, Vol 1697, Springer, 325–432, doi:10.1007/BFb0096355.

——, and S. Osher, 1988: Efficient implementation of essentially non-oscillatory shock-capturing schemes. *J. Comput. Phys.*, **77**, 439–471, doi:10.1016/0021-9991(88)90177-5.

Skamarock, W. C., 2004: Evaluating mesoscale NWP models using kinetic energy spectra. *Mon. Wea. Rev.*, **132**, 3019–3032, doi:10.1175/MWR2830.1.

——, and J. B. Klemp, 2008: A time-split nonhydrostatic atmospheric model for weather research and forecasting applications. *J. Comput. Phys.*, **227**, 3465–3485, doi:10.1016/j.jcp.2007.01.037.

——, ——, J. Dudhia, D. O. Gill, D. M. Barker, W. Wang, and J. G. Powers, 2005: A description of the Advanced Research WRF version 2. NCAR Tech. Note NCAR/TN-468+STR, 88 pp., doi:10.5065/D6DZ069T.

Spiteri, R. J., and S. J. Ruuth, 2002: A new class of optimal high-order strong-stability-preserving time discretization methods. *SIAM J. Numer. Anal.*, **40**, 469–491, doi:10.1137/S0036142901389025.

Stolaki, S., M. Haeffelin, C. Lac, J.-C. Dupont, T. Elias, and V. Masson, 2015: Influence of aerosols on the life cycle of a radiation fog event. A numerical and observational study. *Atmos. Res.*, **151**, 146–161, doi:10.1016/j.atmosres.2014.04.013.

Straka, J., R. B. Wilhelmson, L. J. Wicker, J. R. Anderson, and K. K. Droegemeier, 1993: Numerical solutions of a non-linear density current: A benchmark solution and comparisons. *Int. J. Numer. Methods Fluids*, **17**, 1–22, doi:10.1002/fld.1650170103.

Süli, E., and D. F. Mayers, 2003: *An Introduction to Numerical Analysis.* Cambridge University Press, 444 pp.

Tan, K.-A., R. Morison, and L. Leslie, 2005: A comparison of high-order explicit and non-oscillatory finite difference advection schemes for climate and weather models. *Meteor. Atmos. Phys.*, **89**, 251–267, doi:10.1007/s00703-005-0132-0.

Ullrich, P., 2014: Understanding the treatment of waves in atmospheric models. Part 1: The shortest resolved waves of the 1D linearized shallow-water equations. *Quart. J. Roy. Meteor. Soc.*, **140**, 1426–1440, doi:10.1002/qj.2226.

Wang, R., and R. J. Spiteri, 2007: Linear instability of the fifth-order WENO method. *SIAM J. Numer. Anal.*, **45**, 1871–1901, doi:10.1137/050637868.

Xue, M., and A. J. Thorpe, 1991: A mesoscale numerical model using the nonhydrostatic pressure-based sigma-coordinate equations: Model experiments with dry mountain flows. *Mon. Wea. Rev.*, **119**, 1168–1185, doi:10.1175/1520-0493(1991)119<1168:AMNMUT>2.0.CO;2.

——, K. K. Droegemeier, and V. Wong, 2000: The Advanced Regional Prediction System (ARPS)—A multi-scale nonhydrostatic atmospheric simulation and prediction model. Part I: Model dynamics and verification. *Meteor. Atmos. Phys.*, **75**, 161–193, doi:10.1007/s007030070003.

Zerroukat, M., N. Wood, and A. Staniforth, 2002: SLICE: A semi-Lagrangian inherently conserving and efficient scheme for transport problems. *Quart. J. Roy. Meteor. Soc.*, **128**, 2801–2820, doi:10.1256/qj.02.69.